International Journal of Solids and Structures 282 (2023) 112448

Contents lists available at ScienceDirect

International Journal of Solids and Structures

journal homepage: www.elsevier.com/locate/ijsolstr

Non-spherical axisymmetric deformations of hyperelastic shells

Eran Ben-Haim, Yizhar Or, Amir D. Gat, Gal Shmuel *

Faculty of Mechanical Engineering, Technion –Israel Institute of Technology, Haifa 3200003, Israel

ARTICLE INFO

Keywords:
Nonlinear elasticity
Hyperelastic
Shell
Membrane
Non-spherical deformation
Solid–fluid interaction

ABSTRACT

Spherical elastic shells commonly appear both in nature and man-made devices. Often, their functionality is governed by an incoming- or outgoing flux of fluid. The transient traction that the fluid exerts in the process causes the shell to depart from sphericity. Here, we develop a framework for determining non-spherical axisymmetric deformations, by combining tools from nonlinear continuum mechanics, structural mechanics, and asymptotic analysis. We apply our framework to analyze an exemplary problem of a Mooney–Rivlin shell that is filled by viscous fluid. Collectively, our framework and the insights gained from its application, promote the understanding of the mechanics of such fluid-filled deformable membranes and shells.

1. Introduction

The usage of elastic shell is prevalent in various applications, ranging from bio-engineering and medical devices (Yang et al., 2017; Yamamoto et al., 2001; Ismail et al., 2022; Humphrey, 2013; Milic-Emili et al., 1964) through civil structures to space applications (Jenkins, 2001; Akita et al., 2018). Often, these shell encapsulate gas or liquid, whose interaction with the deformable solid dictates its functionality, through the inflation or deflation of the shell (Siéfert et al., 2019; Manfredi et al., 2019; Bortot and Shmuel, 2018; Ben-Haim et al., 2020, 2022).

The modeling of such fluid-filled elastic shell is a complicated task, owing to the geometrical and material nonlinearities in the response of the solid (Gamus et al., 2017; Corneliussen and Shield, 1961; Foster, 1967; Hart-Smith and Crisp, 1967; Firouzi and Żur, 2022; Shmuel, 2015; Shmuel and DeBotton, 2013), triggered by the solid–fluid interaction (Coussios and Roy, 2008; Yang and Church, 2005; Gaudron et al., 2020; Cassels et al., 2001; Firouzi and Żur, 2022). The majority of works in this field restrict attention to spherical deformations and/or uniform loadings (Yang and Feng, 1970; Treloar, 1975; Beatty, 1987; Hines et al., 2017; Needleman, 1977; Rivlin, 1948; DeBotton et al., 2013; Adkins and Rivlin, 1952; Ben-Haim et al., 2020; Verron et al., 1999; Ilssar and Gat, 2020; Dorfmann and Ogden, 2010). However, while the assumption that the fluid generates uniform pressure on the shell allows for analytical solutions, it fails to describe the transient response of the shell during its filling process by the fluid (Ben-Haim et al., 2022; Ilssar and Gat, 2020); and the few works that go beyond spherical deformations focus on contact problems of elastic membranes and rigid substrates (Flory et al., 2007; Srivastava and Hui, 2013; Liu et al., 2018; Li et al., 2022); bifurcation problems (Haughton and Ogden, 1978; Melnikov et al., 2020); and bulging problems (Xiang et al., 2005; Small and Nix, 1992; Poilâne et al., 2000). There are additional works that calculate the response of the fluid at prescribed non-spherical deformations of the membrane (Brenner, 1964; Klughammer et al., 2018), or study the statistical mechanics of active closed shells or vesicles (Kulkarni, 2023), in cases where the configuration of the shell is assumed to be known.

Here, we develop a framework for determining non-spherical axisymmetric deformations of the shell, and apply it for an exemplary problem of inflation and deflation sphere by viscous fluid. To this end, we combine tools from nonlinear continuum mechanics, structural mechanics, and asymptotic analysis, in the following order.

(*i*) We begin by revisiting the classical spherical solutions (DeBotton et al., 2013; Ogden, 1972) obtained using the theory of nonlinear elasticity (Holzapfel, 2000; Green, 1954); and specialize them for thin shells that are governed by a rather general form of constitutive equations, incl.

(*ii*) We employ these solutions as fictitious auxiliary configuration, with respect to which we model asymmetric deformations as a superposition of incremental deformations on top of large spherical deformations (Baek et al., 2007). This so-called *small-on-large* approach is based on our assumption regarding the transient traction that the fluid exerts, namely, that its nonuniform part is an order of magnitude smaller than its uniform part. We further assume that this pressure is independent of the feedback from the shell, which essentially decouples the fluid–solid problems.

(*iii*) Subsequently, we exploit the fact that the shell is thin in order to develop the equations that govern its mechanics *á la* Kirchhoff–Love shell theory (Love, 1888). This is carried out by integration of

* Corresponding author.
E-mail address: meshmuel@technion.ac.il (G. Shmuel).

https://doi.org/10.1016/j.ijsolstr.2023.112448
Received 14 May 2023; Received in revised form 24 July 2023; Accepted 8 August 2023
Available online 23 August 2023
0020-7683/© 2023 Elsevier Ltd. All rights reserved.

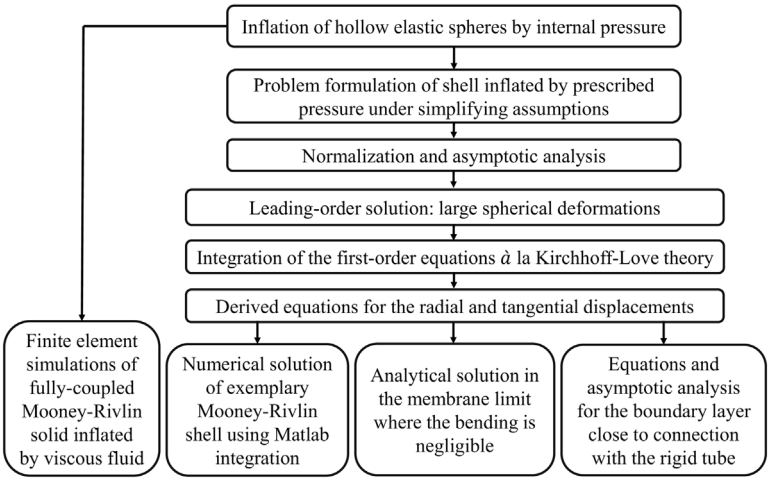

Fig. 1. A chart consisting of the different parts of the work.

the first-order equations, that were obtained after linearization about the auxiliary configuration. After some algebra, we obtain differential equations, which contain bending and tensile terms, for the radial and tangential incremental displacements.

(*iv*) We derive analytical solutions in the membrane limit, where bending is negligible, away from the fixed ends of the solid; near these ends, bending cannot be neglected, and analytical solutions are not accessible.

We demonstrate the applicability of our framework by employing it in exemplary problem of a hollow sphere made of a Mooney–Rivlin solid that is inflated by viscous fluid. We find that the deviation from the spherical configuration is larger when the volume of the incoming flow is larger. Counterintuitively, we further find that the deflation (inflation) of the shell tends to extend (contract) it in the vertical direction while contracting (extending) it in the horizontal direction. We compare our analytical results with fully-coupled COMSOL Multiphysics® finite element simulations (Multiphysics, 1998; Inc., 2020), using its fluid–structure interaction module, in which the exact finite elasticity equations are solved, to find they are in excellent agreement, except near the fixed ends of the solid.

We present our framework and analysis in the following order. In Section 2, we introduce a formal statement of the problem using nonlinear elasticity theory, and develop normalized governing equations based on asymptotic analysis. In Section 3, we revisit the classical spherical solution, and develop the equations that govern non-spherical axisymmetric incremental deformations of the shell with respect to that spherical deformation. We develop in Section 4 the asymptotic approximation to the governing equations of the incremental problem, together with its solution in the membrane limit, where bending moments are negligible. Finally, in Section 5, we apply our framework to an exemplary problem, together with a numerical study of its mechanics. We compare our analytical solution to the membrane equations, with a numerical solution to the shell equations, and finite element solutions to the fully-coupled exact equations, in order to demonstrate the range of applicability of each solution. For convenience, we also provide in Fig. 1 a chart which schematically describes the different parts of our analysis. We conclude this paper with a summary of our main results in Section 6.

2. Problem statement

We consider a thin spherical shell made of an incompressible isotropic elastic material, whose radius in the reference configuration, denoted Ω_R, is R_i, that is connected to a rigid tube of radius a and length ℓ [see Fig. 2(a)–(b)], such that the tube is slender, i.e., $\epsilon_s := a/\ell \ll 1$. We further assume that the shell's radius is much larger than the tube's radius, i.e., the *tube–shell radii ratio* satisfies $\epsilon_a := a/R_i \ll 1$. The shell is subjected to an inhomogeneous traction, p, at its inner boundary, which has the form of a uniform radial component plus a non-uniform component whose magnitude is of one order smaller than the uniform component. (This separation of order of magnitudes is justified by the slenderness of the tube and the small tube–shell radii ratio; for more details, see the work of Ben-Haim et al. (2022).) Our objective is to determine the resultant non-spherical deformation of the shell. This deformation, denoted by χ, maps material points from a reference coordinate $\mathbf{X}$, to their current coordinate $\mathbf{x}$, such that $\mathbf{x} = \chi(\mathbf{X})$. Based on our assumption of the structure of p, it is useful to introduce an intermediate configuration, denoted by Ω_0, that corresponds to the spherical deformation of the shell if the internal traction was uniform and the tube was not rigid, but inflates in a way that maintains the spherical configuration [Fig. 2(c)]. We clarify this configuration is fictitious, and used as an auxiliary, with respect to which we decompose the actual, non-spherical deformation, reached by imposing suitable displacements on the connection points, as described later. The mapping from Ω_R to Ω_0 is denoted by χ_0, such $\mathbf{x}_0 = \chi_0(\mathbf{X})$, and the mapping from Ω_0 to Ω is denoted by $\chi'(\mathbf{x_0})$. Hence, the current position $\mathbf{x}$ can be written as $\mathbf{x} = \mathbf{x}_0 + \mathbf{u}$, where $\mathbf{u}$ is the displacement field with respect to Ω_0. The corresponding *deformation gradient* tensors associated with Ω_0 and Ω are $\mathbf{F}_0 = \nabla_{\mathbf{X}}\chi_0$ and $\mathbf{F} = \nabla_{\mathbf{X}}\chi$, respectively. The relation between the above deformation gradients is $\mathbf{F} = (\mathbf{I} + \mathbf{H})\mathbf{F}_0$, where $\mathbf{H} = \nabla_{\mathbf{x}_0}\mathbf{u}$, and $\mathbf{I}$ is the identity tensor. Owing to the incompressible constraint, we have that identically $\det\mathbf{F} = 1$ and $\mathrm{tr}\mathbf{H} = 0$.

The *Cauchy stress tensor* that evolves in the hyperelastic, isotropic incompressible solid is given by the constitutive relation

$$\boldsymbol{\sigma} = -\mathcal{L}\mathbf{I} + 2\mathbf{F}\frac{\partial\psi}{\partial\mathbf{C}}\mathbf{F}^T, \tag{1}$$

where $\psi(\mathbf{C})$ is the *strain energy density function*, $\mathbf{C} = \mathbf{F}^\mathbf{T}\mathbf{F}$, and $\mathcal{L}$ is a Lagrange multiplier that accounts for the incompressibility constraint. In terms of $\boldsymbol{\sigma}$, the balance of linear momentum is

$$\boldsymbol{\nabla}_{\mathbf{x}}\cdot\boldsymbol{\sigma} = \mathbf{0}. \tag{2}$$

2.1. Normalized formulation and asymptotic analysis

In what follows, we denote by $\{R, \Theta, \Phi\}$ and $\{r, \theta, \phi\}$ the spherical coordinates of a material point in Ω_R and Ω, respectively. Here, θ is the polar angle, measured from the axis of symmetry to the radial coordinate r, and ϕ is the azimuthal angle, revolving around the axis of symmetry, z. Note that the origin of the spherical coordinate is located at the center of the spherical shell.

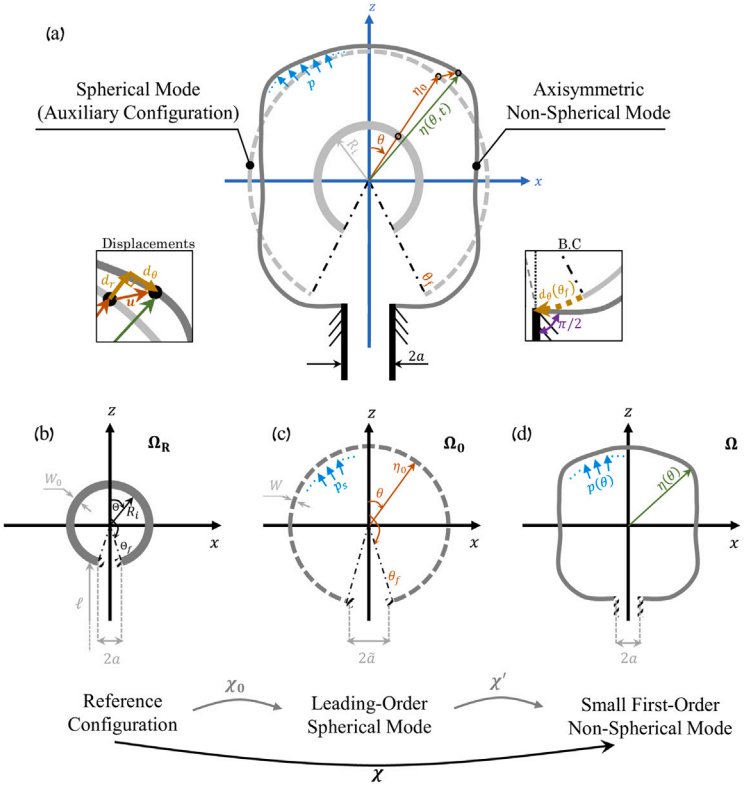

Fig. 2. (a) Illustration of a hyperelastic shell connected to a rigid tube and subjected to prescribed inhomogeneous traction. The thick line represents the initial non-inflated state, i.e., the reference configuration; the dashed line represents the auxiliary configuration where the shell maintains a spherical mode, and the smooth line indicates the non-spherical axisymmetric mode of the inflated shell. Those three elastic configurations are shown separately in - (b) the reference configuration, Ω_R; (c) a finitely deformed intermediate configuration, Ω_0; and (d) the final asymmetric configuration, Ω. The initial inner radius of the shell is R_i, and W_0 is its initial thickness . The tube's length is denoted by ℓ, and the angle of the connection points between the shell and the tube is denoted by $\Theta_f = \theta_f$, which takes a role in the reference and spherical modes. The intermediate spherical configuration results from the uniform pressure p_s, leading to the inner radius η_0 which marked by the orange arrow. The final configuration results from the non-uniform total pressure $p(\theta)$, which is a sum of the leading-order uniform component and a higher-order spatially varying component. The distance of the shell from the origin is denoted by η, which is marked by a green arrow. The right-framed figure (labeled as "B.C") describes the kinematic boundary conditions in the shell–tube connection, and the left-framed figure (labeled as "Displacements") describes the components of the non-spherical displacement vector in the radial and tangential directions.

In the sequel, we employ the slenderness assumption ($\epsilon_s = a/\ell \ll 1$), and further assume that the thickness of the shell is much smaller that its inner radius, i.e., accordingly define $\epsilon_w := W_0/R_i \ll 1$, in order to use these two small parameters in our asymptotic analysis.

It is useful to further introduce the following normalized quantities:

$$\hat{\nabla} = R_i \nabla, \quad \hat{r} = \frac{r}{R_i}, \quad \hat{\mathbf{x}} = \frac{\mathbf{x}}{R_i}, \quad \lambda = \frac{\eta}{R_i}; \tag{3a}$$

$$\hat{\sigma}_{rr} = \frac{\sigma_{rr}}{p^*}, \quad \hat{\sigma}_{r\theta} = \frac{\sigma_{r\theta}}{\tau^* p^*}, \quad \hat{\sigma}_{\theta\theta} = \frac{\sigma_{\theta\theta}}{p^*/\epsilon_w}, \quad \hat{\sigma}_{\phi\phi} = \frac{\sigma_{\phi\phi}}{p^*/\epsilon_w}, \tag{3b}$$

where p^* is the characteristic radial loading, τ^* refers to a scaling parameter that will determined by the boundary condition of the inner shell, $\eta(\theta;t)$ is the distance between the non-spherical shell and the center of the spherical shell, $\hat{r}$ is the normalized radial coordinate, and $\lambda(\theta;t)$ is the distance to the non-spherical shell, normalized by the reference inner radius [Fig. 2(d)]. According to our assumption on the structure of p, we expand the normalized internal non-uniform loading as follows[1]

$$\hat{p}\big(\hat{r} = \lambda(\theta)\big) \sim \hat{p}_s(\lambda_0) + \epsilon_s \hat{p}_d(\lambda_0, \theta) + \mathcal{O}(\epsilon_s^2), \tag{4}$$

where $\hat{p} = p/p^*$ is the normalized inner loading, $\hat{p}_s(\lambda_0)$ is the uniform radial traction, and $\epsilon_s \hat{p}_d(\lambda_0, \theta)$ is the small non-uniform component. This assumption allows us to decompose λ according to $\lambda(\theta) = \lambda_0 + \epsilon_s \lambda_1(\theta) + \mathcal{O}(\epsilon_s^2)$ where $\lambda_0 = \eta_0/R_i$ is the radial stretch at the intermediate spherical configuration , η_0 is the radius of the shell at the intermediate configuration, and λ_1 is a first-order term that depends on the non-uniform part of the inner pressure. We recall in this process, we assumed that the pressure is known, i.e., we neglected the feedback from the solid. For more details, see Appendix D.4.

The assumption that the intermediate and current configurations are close allows us to obtain the following perturbation of the current position

$$\hat{\mathbf{x}}(\mathbf{X}) = \hat{\mathbf{x}}_0(\mathbf{X}) + \epsilon_s \hat{\mathbf{u}}\big(\hat{\mathbf{x}}_0(\mathbf{X})\big) + \mathcal{O}(\epsilon_s^2), \tag{5}$$

where $\hat{\mathbf{u}} = \hat{d}_r(\hat{r}, \theta)\mathbf{e}_\mathbf{r} + \hat{d}_\theta(\hat{r}, \theta)\mathbf{e}_\theta$, and $\hat{d} = d/R_i\epsilon_s$ are the normalized non-spherical displacements. This normalization allows us to obtain a form in which the small parameter ϵ_s is explicit[2]. Owing to relation (5), the gradients of the successive deformation can be written as (Baek et al., 2007)

$$\mathbf{F} = \mathbf{F}_0 + \epsilon_s \mathbf{F}_1 + \mathcal{O}(\epsilon_s^2), \tag{6}$$

where $\mathbf{F}_1 = \mathbf{H}\mathbf{F}_0$. Substituting Eq. (6) into the definition of $\mathbf{C}$ provides

$$\mathbf{C} = \mathbf{C}_0 + \epsilon_s \mathbf{C}_1 + \mathcal{O}(\epsilon_s^2), \tag{7}$$

[1] Mathematically, since we assume that p has a prescribed form, the tube slenderness assumption is not needed. However, the tube's slenderness provides a physical justification to this form.

[2] Owing to the assumption that $\mathbf{u}$ is of a different order than $\mathbf{x}$, its corresponding dimensionless form is scaled differently, namely, by $\epsilon_s R_i$, such the ϵ_s terms cancel out when recovering back the dimensional equation.

where $\mathbf{C}_0 = \mathbf{F}_0^T\mathbf{F}_0$ and $\mathbf{C}_1 = \mathbf{F}_0^T\mathbf{H}\mathbf{F}_0 + \mathbf{F}_0^T\mathbf{H}^T\mathbf{F}_0 = 2\mathbf{F}_0^T\mathbf{e}\mathbf{F}_0$ where $\mathbf{e} = (\mathbf{H}+\mathbf{H}^T)/2$ is the small strain tensor with respect to the intermediate configuration. We assume that the normalized Cauchy stress tensor can also be written in a similar form, namely,

$$\hat{\boldsymbol{\sigma}} = \hat{\boldsymbol{\sigma}}^{(0)} + \epsilon_s\hat{\boldsymbol{\sigma}}^{(1)} + \mathcal{O}(\epsilon_s^2), \tag{8}$$

where $\hat{\boldsymbol{\sigma}}^{(0)}$ is the non-dimensional Cauchy stress tensor that evolves in the intermediate spherical configuration, and $\hat{\boldsymbol{\sigma}}^{(1)}$ is the additional non-dimensional Cauchy stresses created from the non-spherical mode.

By linearizing Eq. (1) about $\mathbf{C}_0$, we have that

$$\hat{\boldsymbol{\sigma}}^{(0)} = -\hat{\mathcal{L}}^{(0)}\mathbf{I} + 2\mathbf{F}_0\frac{\partial\hat{\psi}}{\partial\mathbf{C}}\bigg|_{\mathbf{C}_0}\mathbf{F}_0^T, \tag{9a}$$

$$\hat{\boldsymbol{\sigma}}^{(1)} = -\hat{\mathcal{L}}^{(1)}\mathbf{I} + 2\mathbf{F}_0\frac{\partial\hat{\psi}}{\partial\mathbf{C}}\bigg|_{\mathbf{C}_0}\mathbf{F}_0^T\mathbf{H}^T + 2\mathbf{H}\mathbf{F}_0\frac{\partial\hat{\psi}}{\partial\mathbf{C}}\bigg|_{\mathbf{C}_0}\mathbf{F}_0^T + 2\mathbf{F}_0\frac{\partial^2\hat{\psi}}{\partial\mathbf{C}^2}\bigg|_{\mathbf{C}_0}\mathbf{C}_1\mathbf{F}_0^T, \tag{9b}$$

where $\hat{\psi} = \psi/\psi^*$ is the free energy function normalized with respect to the characteristic magnitude and $\hat{\mathcal{L}}^{(\cdot)} = \mathcal{L}^{(\cdot)}/\psi^*$ is the normalized Lagrange multiplier.

3. Solution of the finite deformation and analysis of superposed deformations

In this section, we first revisit the solution of the finite spherical deformation. For this purpose, we use the thin-shell approximation to determine the leading-order relationship between the stretch of the shell and the inner uniform traction. Subsequently, we analyze the non-spherical deformation that is superimposed on the finite deformation. To do so, we analyze the first-order Cauchy stress that is generated and rewrite the instantaneous constitutive relations in Hook's law-like form. Then, we develop the balance equations and boundary conditions that govern the non-spherical incremental stress in the shell relative to its spherically inflated state using a Kirchhoff–Love approximation.

In the sequel, we restrict attention to materials that are governed by constitutive relation of the form

$$\hat{\psi}(\mathbf{C}) = \hat{\Psi}(I_1(\mathbf{C})) + \hat{\varphi}(I_2(\mathbf{C})), \tag{10}$$

such that $\hat{\Psi}$ is a possibly nonlinear function of I_1, while $\hat{\varphi}$ must be a linear function of I_2, where

$$I_1 = \operatorname{tr}\mathbf{C}, \quad \text{and} \quad I_2 = \frac{1}{2}\left[(\operatorname{tr}\mathbf{C})^2 - \operatorname{tr}(\mathbf{C}^2)\right], \tag{11}$$

are the invariants of $\mathbf{C}$. Note that a large number of popular models for rubber admit form Eq. (10), such as Treloar (1943), Mooney (1940), Gent (1996), and Yeoh models (Yeoh, 1993; Ogden, 1972). We emphasize that our framework and specifically the governing equations to be derived, apply to all of these models. In the numerical section to follow, we use by way of example the Mooney–Rivlin solid.

3.1. Non-linear large spherical deformation of the shell

The solution to the nonlinear problem is given by Green (1954), see also the works of DeBotton et al. (2013) and Ogden (1972). We summarize its thin shell version here, for completeness. For convenience, we normalize the reference radial coordinate according to $\hat{R} = R/R_i$. Accordingly, $\hat{R} = 1$ to the leading order, and to the first order $\hat{R} \in [1, 1+\epsilon_w]$.

Owing to the spherical symmetry of the problem and the incompressibility constraint, the finite deformation is given by

$$\hat{r} = \sqrt[3]{\lambda_0^3 + \hat{R}^3 - 1}, \quad \theta = \Theta, \quad \phi = \Phi, \tag{12}$$

where $\lambda_0 \leqslant \hat{r} \leqslant \lambda_0 + \epsilon_w\lambda_0^{-2} + \mathcal{O}(\epsilon_w^2)$, and $\theta \in [0, \theta_f]$ where θ_f is the angle to the connection points with the tube. We recall that here, we fictitiously allow the tube to deform in a way that is compatible with the spherical deformation of the shell, such that its radius increases to $\tilde{a} = \lambda_0 a$ [see Fig. 2(c)]. This fictitious displacement of the tube is accounted for in the calculation of the final deformation. We further recall that λ_0 is to be determined from the boundary conditions. Owing to the thin shell assumption and the fictitious compatibility of the tube, to the leading order, the deformation gradient is constant and diagonal, having the following representation in our coordinate system $\mathsf{F}_0 = \operatorname{diag}[\lambda_0^{-2}, \lambda_0, \lambda_0]$, and thus $\mathsf{C}_0 = \operatorname{diag}[\lambda_0^{-4}, \lambda_0^2, \lambda_0^2]$.

Under the assumption of a shell made of a material that is governed by Eq. (10), the resultant stress is given by

$$\hat{\boldsymbol{\sigma}}^{(0)} = -\hat{\mathcal{L}}^{(0)}\mathbf{I} + 2\left(\hat{\psi}_1 + \hat{\psi}_2 I_1^{(0)}\right)\mathbf{C}_0 - 2\hat{\psi}_2\mathbf{C}_0^2, \tag{13}$$

where

$$\hat{\psi}_i \equiv \frac{\partial\hat{\psi}}{\partial I_i}\bigg|_{\left(I_1^{(0)}, I_2^{(0)}\right)}; \qquad i = 1, 2, \tag{14}$$

and $I_i^{(0)} \equiv I_i(\mathbf{C}_0)$. The only non-trivial balance of the linear momentum equation is in the radial direction, which has the normalized form

$$\epsilon_w\frac{\mathrm{d}\hat{\sigma}_{rr}^{(0)}}{\mathrm{d}\hat{r}} + \frac{2}{\hat{r}}\left(\epsilon_w\hat{\sigma}_{rr}^{(0)} - \hat{\sigma}_{\theta\theta}^{(0)}\right) = 0. \tag{15}$$

Eq. (15) is to be solved in conjunction with the boundary conditions, which are a traction-free outer boundary and a prescribed inner uniform pressure, $\hat{p}_s$.

The boundary condition at the outer surface leads to the equation $\hat{\sigma}_{rr}^{(0)} = 0$ at $\hat{r} \sim \lambda_0 + \epsilon_w\lambda_0^{-2}$, from which we obtain that the Lagrange multiplier $\hat{\mathcal{L}}^{(0)}$ satisfies

$$\hat{\mathcal{L}}^{(0)} = 2\left(\lambda_0^{-4}\hat{\psi}_1 + 2\lambda_0^{-2}\hat{\psi}_2\right) + \mathcal{O}(\epsilon_w). \tag{16}$$

Next, we integrate Eq. (15) with respect to $\hat{r}$ from λ_0 to $\lambda_0 + \epsilon_w\lambda_0^{-2}$, and use the equation that results from the inner boundary condition, namely,

$$\hat{\sigma}_{rr}^{(0)} = -\hat{p}_s(\lambda_0), \tag{17}$$

to find that

$$\hat{p}_s(\lambda_0) = 2\lambda_0^{-3}\hat{\sigma}_{\theta\theta}^{(0)} + \mathcal{O}(\epsilon_w). \tag{18}$$

Relations (13)–(18) provide

$$\hat{p}_s(\lambda_0) = 4\left[\left(\lambda_0^{-1} - \lambda_0^{-7}\right)\hat{\psi}_1 + \left(\lambda_0 - \lambda_0^{-5}\right)\hat{\psi}_2\right] + \mathcal{O}(\epsilon_w) = \frac{1}{\lambda_0^2}\frac{\mathrm{d}\hat{\psi}}{\mathrm{d}\lambda_0} + \mathcal{O}(\epsilon_w). \tag{19}$$

The latter relation is in agreement with the works of Beatty (1987) and Ogden (1972). In the next subsection, we develop the equations that govern the non-spherical incremental deformations of the shell, relatively to this spherically inflated state, using a thin-shell approximation.

3.2. Small-on-large non-spherical axisymmetric deformations

We begin by deriving the instantaneous constitutive relations of the shell about its spherical state. To this end, we recall that the relative displacement gradient $\mathbf{H}$ that appears in the incremental constitutive law (9b) is

$$H = \begin{bmatrix} H_{rr} & H_{r\theta} & 0 \\ H_{\theta r} & H_{\theta\theta} & 0 \\ 0 & 0 & H_{\phi\phi} \end{bmatrix} = \begin{bmatrix} \frac{\mathrm{d}\hat{d}_r}{\mathrm{d}\hat{r}} & \frac{1}{\hat{r}}\left(\frac{\mathrm{d}\hat{d}_r}{\mathrm{d}\theta} - \hat{d}_\theta\right) & 0 \\ \frac{\mathrm{d}\hat{d}_\theta}{\mathrm{d}\hat{r}} & \frac{1}{\hat{r}}\left(\hat{d}_r + \frac{\mathrm{d}\hat{d}_\theta}{\mathrm{d}\theta}\right) & 0 \\ 0 & 0 & \frac{1}{\hat{r}}\left(\hat{d}_r + \hat{d}_\theta\cot\theta\right) \end{bmatrix}. \tag{20}$$

This constitutive relation can be reduced to a Hook's law-like form at a given λ_0, using the boundary conditions. Specifically, since the outer boundary is free of traction, it follows that $\hat{\sigma}_{rr}^{(1)}$ vanishes at the outer boundary, which allows us to calculate $\hat{\mathcal{L}}^{(1)}$, namely,

$$\hat{\mathcal{L}}^{(1)} = -4\left[\left(\lambda_0^{-8} - \lambda_0\right)\hat{\psi}_{11} + \lambda_0^{-4}\hat{\psi}_1 + \left(2\lambda_0^{-2} - \lambda_0\right)\hat{\psi}_2\right]H_{rr} + \mathcal{O}(\epsilon_w). \tag{21}$$

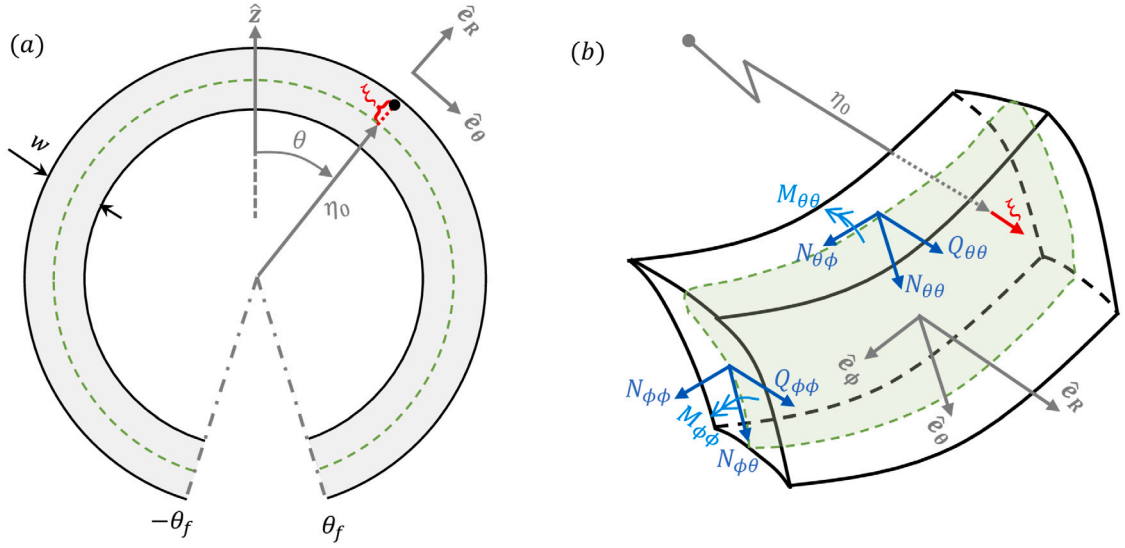

Fig. 3. (a) A cut of the shell in the intermediate spherical configuration, whose thickness is w. The green dashed line represents the middle surface element of the thin spherical shell, and ξ is the radial distance from the middle surface. (b) A differential spherical element and its associated stress resultants N, transverse shear stress resultants Q, and stress couples M.

Substituting it back into the constitutive law (9b) provides

$$\begin{bmatrix}\hat{\sigma}^{(1)}_{\theta\theta}\\ \hat{\sigma}^{(1)}_{\phi\phi}\end{bmatrix} = \frac{\tilde{E}(\lambda_0)}{1-\tilde{\nu}^2(\lambda_0)}\begin{bmatrix}1 & \tilde{\nu}(\lambda_0)\\ \tilde{\nu}(\lambda_0) & 1\end{bmatrix}\begin{bmatrix}e_{\theta\theta}\\ e_{\phi\phi}\end{bmatrix}, \tag{22}$$

where the explicit expressions of $\tilde{E}(\lambda_0)$ and $\tilde{\nu}(\lambda_0)$ are given in Appendix B.

Having Eq. (22) at hand, we proceed to derive the balance equation in terms of $e_{\theta\theta}$ and $e_{\phi\phi}$, using a shell theory approach. We recall that such an approach is applicable when the normal stress is negligible, i.e., $\hat{\sigma}^{(1)}_{rr} \ll \hat{\sigma}^{(1)}_{\theta\theta}, \hat{\sigma}^{(1)}_{\phi\phi}$, and that normals to the shell's reference natural surface remain normal. Then, it follows that we can describe the relative displacement gradient field in terms of its values at the middle plane and the distance from it: this is Love–Kirchhoff's assumption. Accordingly, we define $\xi \in [-w/2, w/2]$ as the radial position measured from the middle surface [Fig. 3(a)].

We introduce the stress resultants $N_{\theta\theta}$ and $N_{\phi\phi}$, transverse shear stress resultant $Q_{\theta\theta}$, and the stress couples $M_{\theta\theta}$ and $M_{\phi\phi}$, defined by Ventsel et al. (2002) and Beuthe (2008):

$$N_{(i)(i)} = \int_{-w/2}^{w/2}\left(1+\frac{\xi}{\eta_0}\right)\sigma^{(1)}_{(i)(i)}\mathrm{d}\xi, \quad Q_{\theta\theta} = \int_{-w/2}^{w/2}\left(1+\frac{\xi}{\eta_0}\right)\sigma^{(1)}_{r\theta}\mathrm{d}\xi,$$
$$M_{(i)(i)} = \int_{-w/2}^{w/2}\left(1+\frac{\xi}{\eta_0}\right)\sigma^{(1)}_{(i)(i)}\xi\mathrm{d}\xi, \tag{23}$$

where $i = \theta, \phi$, in terms of which we rewrite the equilibrium equation; the explicit expressions for the terms in Eq. (23) are given in Appendix B.

The solution to the leading order of the balance equations is given in Section 3.1, and in what follows, we tackle the first-order equations. In order to express them in terms of N, Q and M, we multiply the radial equation by $(\eta_0+r)^2\sin\theta$ and the polar equation by $(\eta_0+r)\sin\theta$. We integrate the resultant equations with respect to r and obtain

$$\frac{\mathrm{d}}{\mathrm{d}\theta}\left(Q_{\theta\theta}\sin\theta\right) - \left(N_{\theta\theta}+N_{\phi\phi}\right)\sin\theta + \eta_0(p-p_s)\sin\theta = 0, \tag{24a}$$

$$\frac{\mathrm{d}}{\mathrm{d}\theta}\left(N_{\theta\theta}\sin\theta\right) - N_{\phi\phi}\cos\theta + Q_{\theta\theta}\sin\theta = 0, \tag{24b}$$

where $p-p_s = \epsilon_s p^* \hat{p}_s$. The third equation is derived by multiplying the polar equation by r and integrating over the thickness, resulting with

$$\frac{\mathrm{d}}{\mathrm{d}\theta}\left(M_{\theta\theta}\sin\theta\right) - M_{\phi\phi}\cos\theta - \eta_0 Q_{\theta\theta}\sin\theta = 0. \tag{25}$$

The remaining azimuthal equation is satisfied identically. After some tedious algebra, as detailed in Appendix C, we obtain the following non-dimensional equations for $\hat{d}_r$ and $\hat{d}_\theta$, namely,

$$\frac{\epsilon_w^2}{12\lambda_0^6\left(1-\tilde{\nu}^2(\lambda_0)\right)}\left[\left(\mathcal{T}_\theta-2\right)\mathcal{T}_\theta^2\right]\hat{d}_r + \mathcal{T}_\theta\hat{d}_r = \frac{\lambda_0^4}{\tilde{E}(\lambda_0)}\left[\mathcal{T}_\theta - \left(1+\tilde{\nu}(\lambda_0)\right)\right]\hat{p}_d, \tag{26}$$

and

$$\left[\mathcal{T}_\theta - \left(1+\tilde{\nu}(\lambda_0)\right)\right]\hat{d}_\theta = -\left(1+\tilde{\nu}(\lambda_0)\right)\frac{\mathrm{d}\hat{d}_r}{\mathrm{d}\theta} + \frac{\epsilon_w^2}{12\lambda_0^2}\frac{\mathrm{d}}{\mathrm{d}\theta}\mathcal{T}_\theta\hat{d}_r, \tag{27}$$

where $\mathcal{T}_\theta$ is a linear differential operator defined by

$$\mathcal{T}_\theta\{\bullet\} \equiv \frac{1}{\sin\theta}\frac{\mathrm{d}}{\mathrm{d}\theta}\left(\sin\theta\frac{\mathrm{d}}{\mathrm{d}\theta}\{\bullet\}\right) + 2\{\bullet\} = \frac{\mathrm{d}^2}{\mathrm{d}\theta^2}\{\bullet\} + \cot\theta\frac{\mathrm{d}}{\mathrm{d}\theta}\{\bullet\} + 2\{\bullet\}. \tag{28}$$

Eq. (26) constitutes a sixth-order ordinary differential equation (ODE) for $\hat{d}_r$, which has the classical form of an ODE that yields a solution of boundary layer structure. Specifically, the first term on the left-hand side is associated with the bending of the shell near the fixed end of the tube, and the second term on the left-hand side is an ODE of a membrane under pure tension. Solving Eqs. (26) and (27) requires six and two boundary conditions, respectively, which we specify next.

3.3. Boundary conditions

The fact that the shell is fixed at the connection points between the shell and the tube implies that

$$\hat{d}_r\big|_{\theta=\theta_f} = 0. \tag{29}$$

Furthermore, the angle between the shell and the tube is fixed to $\pi/2$, and hence

$$\frac{\mathrm{d}\hat{d}_r}{\mathrm{d}\theta}\bigg|_{\theta=\theta_f} = -\frac{\lambda_0}{\epsilon_s}\cot\left(3\pi/2 - \sin^{-1}\left(\epsilon_a/\lambda_0\right)\right) \approx -\frac{\epsilon_a}{\epsilon_s}. \tag{30}$$

Owing to the axial symmetry, all the odd derivatives of the radial displacements at $\theta = 0$ must vanish, i.e.,

$$\frac{\mathrm{d}\hat{d}_r}{\mathrm{d}\theta}\bigg|_{\theta=0} = \frac{\mathrm{d}^3\hat{d}_r}{\mathrm{d}\theta^3}\bigg|_{\theta=0} = \frac{\mathrm{d}^5\hat{d}_r}{\mathrm{d}\theta^5}\bigg|_{\theta=0} = 0. \tag{31}$$

Additionally, to obtain a physical solution, the displacement field must be bounded at $\theta \to 0$.

The solution of Eq. (26) when subjected to the above boundary conditions, is detailed in Section 4. Having this solution at hand, we

proceed to Eq. (27) for $\hat{d}_\theta$. The tangential displacement is subjected to the two boundary conditions

$$\hat{d}_\theta\Big|_{\theta=0} = 0 \quad \text{and} \quad \hat{d}_\theta\Big|_{\theta=\theta_f} \approx (\lambda_0 - 1)\epsilon_a. \tag{32}$$

The first of Eq. (32) results from the axial symmetry; the second of Eq. (32) enforces the total displacement of connections points with rigid tube to be null, thereby canceling their fictitious displacement to the auxiliary configuration [see Fig. 2(a)].

4. Asymptotic approximation solution

While Eqs. (26)–(27) can be solved numerically, it is advantageous to derive an approximated asymptotic solution, with which it is possible to gain insights on the mechanics of the problem; this is carried out next. Our approximation relies on the fact that the solution to Eq. (26) has a boundary layer structure. Accordingly, we divide the solution to two regimes, namely, one that results when retaining only the leading order (so-called *outer solution*), and one that accounts for higher orders (so-called *inner solution*).

The outer solution is identified with a membrane state, at which the shell does not carry bending moments ($M_{\theta\theta}$ and $M_{\phi\phi}$), i.e., the bending rigidity D vanishes [Eq. (B.3)]. However, near the connection with the tube, the fixed end stiffens the response of the shell to bending, and hence this approximation is no longer valid. Therefore, at that regime, we must account for higher-order terms. These two types of solutions are analyzed next.

4.1. Outer solution—Membrane limit

We begin with the outer solution, referred to as the membrane limit. Under this approximation, the resultant equation is

$$\frac{\mathrm{d}^2\hat{d}_r}{\mathrm{d}\theta^2} + \cot\theta\frac{\mathrm{d}\hat{d}_r}{\mathrm{d}\theta} + 2\hat{d}_r \sim \frac{\lambda_0^4\left(1-\tilde{\nu}(\lambda_0)\right)}{\tilde{E}(\lambda_0)}\hat{p}_d, \tag{33}$$

where we neglect pressure derivatives under the assumption that they are small enough in the outer regime. Eq. (33) has an analytical solution that is constrained by two boundary conditions, associated with two integration constants. One of these constants multiplies an expression that is singular at $\theta \to 0$; hence this constant must be null. It follows that the remaining term satisfies identically the boundary condition $\mathrm{d}\hat{d}_r/\mathrm{d}\theta = 0$ at $\theta \to 0$, and therefore an addition boundary condition is required: this second condition is the *Prandtl matching condition* (Vasil'Eva et al., 1995; Gao and Krysko, 2006).

Accordingly, the analytical solution in the outer regime is

$$\begin{aligned}\hat{d}_r(\theta) \sim &\left[C_1 + \frac{\lambda_0^4\left(1-\tilde{\nu}(\lambda_0)\right)}{\tilde{E}(\lambda_0)}\int_{\cos\theta}^1\left(1+\frac{\xi}{2}\ln\left(\frac{1-\xi}{1+\xi}\right)\right)\hat{p}_d\left(\cos^{-1}(\xi)\right)\mathrm{d}\xi\right]\cos\theta + \\ &+ \frac{\lambda_0^4\left(1-\tilde{\nu}(\lambda_0)\right)}{\tilde{E}(\lambda_0)}\left(1+\frac{\cos\theta}{2}\ln\left(\frac{1-\cos\theta}{1+\cos\theta}\right)\right)\int_{\cos\theta}^1\hat{p}_d\left(\cos^{-1}(\xi)\right)\mathrm{d}\xi,\end{aligned} \tag{34}$$

where $C_1 = \hat{d}_r(0)$ is the constant to be determined from Prandtl matching condition. We note that in the numerical examples to follow, we have determined $\hat{d}_r(0)$ using COMSOL finite element simulations.

4.2. Inner solution—Boundary layer

In order to analyze the equation that is associated with the inner regime, we employ the local analysis method. To this end, we assume that at θ_f, the size of the boundary layer is of order $\delta \ll 1$. In this vicinity, we rescale the coordinate θ by introducing the local variable

$$\xi = \frac{\theta_f - \theta}{\delta} \sim \mathcal{O}(1). \tag{35}$$

Table 1
The mechanical properties that are used in our numerical study. The density and kinematic viscosity of the fluid are associated with Glycerol. The geometrical parameters are the typical values used by Ben-Haim et al. (2020).

Parameters	Notation	Value	Units
Density	ρ	1260	Kg/m^3
Dynamic Viscosity	μ	1.1	Pa s
Elastic Parameter	s_1	1.5	MPa
Elastic Parameter	s_2	0.15	MPa
Unstressed Radius	R_i	5	mm
Unstressed Thickness	W_0	50	μm
Tube radius	a	1	mm
Tube length	ℓ	20	cm
Tube slenderness	ϵ_s	5×10^{-4}	
Tube–shell radii ratio	ϵ_a	2×10^{-2}	
Thick-radius ratio	ϵ_w	1×10^{-4}	
Chamber viscous resistance	ϵ_μ	4×10^{-5}	

Accordingly, with this substitution of variable, we define $\hat{d}_{in}(\xi) \equiv \hat{d}_r(\theta(\xi))$, to which we obtain the derivatives with respect to ξ using the chain rule, namely,

$$\frac{\mathrm{d}^2}{\mathrm{d}\theta^2} + \cot\theta\frac{\mathrm{d}}{\mathrm{d}\theta} \sim \frac{1}{\delta^2}\frac{\mathrm{d}^2}{\mathrm{d}\xi^2} + \frac{1}{\delta(\epsilon_a+\xi\delta)}\frac{\mathrm{d}}{\mathrm{d}\xi}. \tag{36}$$

In the latter relation, we used the first order approximation of $\cot\theta$ at $\theta \to \theta_f$ and $\theta_f \sim \pi - \epsilon_a$. This provides the following equation for $\hat{d}_{in}$

$$\begin{aligned}&\frac{\epsilon_w^2}{12\lambda_0^6\left(1-\tilde{\nu}^2(\lambda_0)\right)}\left(\frac{1}{\delta^2}\frac{\mathrm{d}^2}{\mathrm{d}\xi^2} + \frac{1}{\delta(\epsilon_a+\xi\delta)}\frac{\mathrm{d}}{\mathrm{d}\xi}\right)^3\hat{d}_{in} \\ &\quad\sim \frac{\lambda_0^4}{\tilde{E}(\lambda_0)}\left(\frac{1}{\delta^2}\frac{\mathrm{d}^2}{\mathrm{d}\xi^2} + \frac{1}{\delta(\epsilon_a+\xi\delta)}\frac{\mathrm{d}}{\mathrm{d}\xi}\right)\hat{p}_d.\end{aligned} \tag{37}$$

We further assume that $\epsilon_a^2 \sim \epsilon_w$. This assumption holds as long as the wall thickness is two orders of magnitude smaller than the radius of the body, following the thin shell theory assumption. Furthermore, the entrance opening is one order of magnitude smaller than the radius of the body. Subsequently, by applying the dominant balance of order of magnitude, we find that the boundary layer thickness satisfies $\delta = \sqrt{\epsilon_w}$.

The governing equation for the inner regime becomes

$$\begin{aligned}&\left(\frac{\mathrm{d}^2}{\mathrm{d}\xi^2} + \frac{1}{\xi+\epsilon_a\epsilon_w^{-1/2}}\frac{\mathrm{d}}{\mathrm{d}\xi}\right)^3\hat{d}_{in} \\ &\quad\sim \frac{12\lambda_0^{10}\left(1-\tilde{\nu}^2(\lambda_0)\right)}{\tilde{E}(\lambda_0)}\left(\frac{\mathrm{d}^2}{\mathrm{d}\xi^2} + \frac{1}{\xi+\epsilon_a\epsilon_w^{-1/2}}\frac{\mathrm{d}}{\mathrm{d}\xi}\right)\hat{p}_d.\end{aligned} \tag{38}$$

In contrast with Eq. (34), we were not able to obtain an analytical solution for Eq. (38), and in the sequel we have Matlab numerical integration to solve it.

5. Application for inflation and deflation of Mooney–Rivlin shell by viscous fluid

In this section, we apply the general framework that we developed to study the non-spherical axisymmetric deformations of a hyperelastic shell, that is governed by the incompressible Mooney–Rivlin constitutive law, owing to influx/outflux of an incompressible viscous fluid. The incompressible Mooney–Rivlin model, aimed at capturing the response of rubber-like materials, is (Beatty, 1987; Ogden, 1997)

$$\psi\left(I_1, I_2\right) = s_1(I_1 - 3) + s_2\left(I_2 - 3\right), \tag{39}$$

where $\{s_{1,2}\}$ are two empirically elastic material coefficients, whose average equals the shear modulus in the limit of small strains. Note that in what follows, we use a normalized strain energy density function that is defined by $\hat{\psi} = \psi/s_1$, i.e., $\psi^* = s_1$.

Since the deformation of the shell is driven by the incoming flux of the fluid, here the independent variable is the inlet flux, $q(t)$, generating the non-uniform pressure. In what follows, we will relate $q(t)$ to the

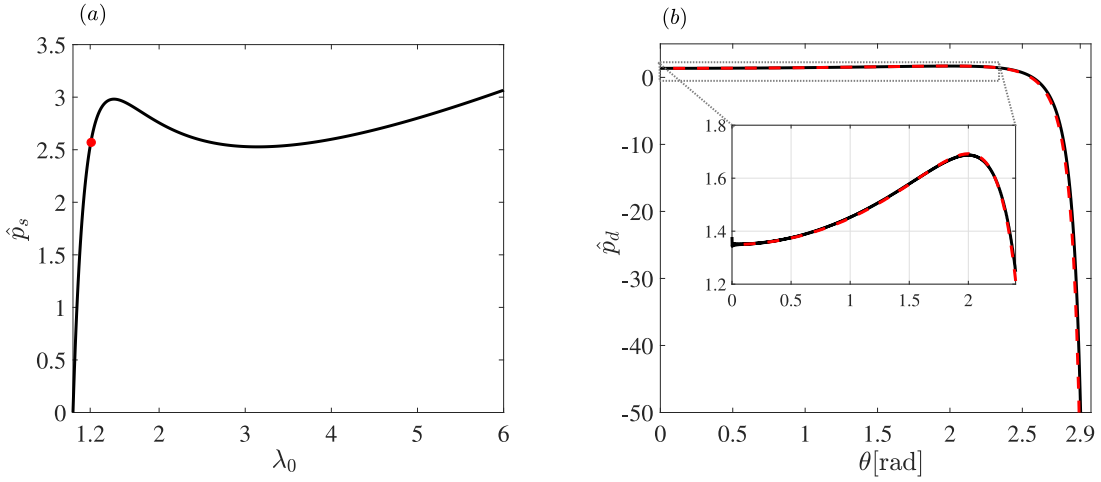

Fig. 4. (a) The pressure–stretch relation (19) of a shell whose properties are given in Table 1. The red mark denotes the configuration that we study in Section 5, where $\lambda_0 = 1.2$. (b) The distribution of the normalized first-order pressure across the inner radius of the shell as a function of θ. The solid black line is the numerical CFD solution, and the dashed red line is the analytical solution (46). The inset highlights that the variation away from the fixed end is an order of magnitude of smaller than the variation near the fixed end.

leading order stretch of the membrane and the corresponding traction. To this end, we employ the integral form of the mass conservation equation, namely,

$$\hat{q}(T) = \frac{d}{dT}\left[\frac{2\pi\epsilon_a^2}{3}\sqrt{\lambda_0^2(T)-\epsilon_a^2} + \int_{\phi=0}^{2}\int_{\theta=0}^{\theta_f}\int_{\hat{r}=0}^{\lambda(\theta,T)} \hat{r}^2\sin\theta \mathrm{d}\hat{r}\mathrm{d}\theta\mathrm{d}\phi\right] \sim \frac{d}{dT}\left[\frac{4}{3}\left(\lambda_0^3(T)-1\right) + 2\epsilon_s\lambda_0^2(T)\int_0^{\theta_f}\hat{d}_r(T;\theta)\sin\theta\mathrm{d}\theta\right] + \mathcal{O}\left(\epsilon_a^4, \epsilon_s^2\epsilon_a^2\right) \tag{40}$$

where $\hat{q} = q(t)/q^*, q^* = \pi a^4 p^*/\mu\ell$ is the normalized volumetric flux rate, μ is the viscosity of the fluid, $T = t/(R_i/v^*)$ is the non-dimensional time, and v^* is the typical flow velocity.[3] Accordingly, to the leading order, i.e., when $\epsilon_s = 0$, we have that the stretch-flux relation is

$$\lambda_0(T) = \left[1 + \frac{3}{4}\int_0^T \hat{q}(\tau)\mathrm{d}\tau\right]^{1/3}. \tag{41}$$

Having determined λ_0 using $\hat{q}(t)$ as per our hypothesis, we now require that

$$\int_0^{\theta_f} \hat{d}_r(\theta;T)\sin\theta\mathrm{d}\theta = 0, \quad \text{for all} \quad T > 0. \tag{42}$$

In the sequel, we will use Eq. (42) as an additional constraint to solve Eq. (26).

Our next step is to calculate the traction that the fluid applies on the shell, which requires a specification of the constitutive law of the fluid. Here, we assume that the fluid is governed by a Newtonian law, namely,

$$\hat{\boldsymbol{\sigma}} = -\hat{p}\mathbf{I} + \epsilon_\mu\left[\hat{\nabla}\hat{\boldsymbol{v}} + \left(\hat{\nabla}\hat{\boldsymbol{v}}\right)^T\right], \tag{43}$$

where $\hat{\boldsymbol{\sigma}} = \boldsymbol{\sigma}/p^*$ is the normalized fluid total stress tensor, $p^* = W_0\psi^*/R_i = \epsilon_w\psi^*$ is the characteristic pressure distribution, $\epsilon_\mu = (a/R_i)^3\epsilon_s \ll \epsilon_s$ is the *chamber viscous resistance* small parameter, $\hat{\boldsymbol{v}} = \boldsymbol{v}/(q^*/\pi R_i^2)$ is the normalized flow velocity field and $\mathbf{I}$ is the identity tensor. Note that $\tau^* = \epsilon_\mu$, [see Eq. (3b)]. Eq. (43) implies that the velocity field contributes only to the first-order term of the stress, and hence the leading order term of the stress in the fluid corresponds to a hydrostatic state. To determine Eqs. (24a)–(24b), it is required to calculate $\hat{\sigma}_{rr}$ and $\hat{\sigma}_{r\theta}$, namely,

$$\hat{\sigma}_{rr} = -\hat{p}_s - \epsilon_s\hat{p}_d + 2\epsilon_\mu\frac{\partial\hat{v}_r}{\partial\hat{r}}, \quad \text{and} \quad \hat{\sigma}_{r\theta} = \epsilon_\mu\left[\hat{r}\frac{\partial}{\partial\hat{r}}\left(\frac{\hat{v}_\theta}{\hat{r}}\right) + \frac{1}{\hat{r}}\frac{\partial\hat{v}_r}{\partial\theta}\right]. \tag{44}$$

Since $\epsilon_\mu \ll \epsilon_s$, we neglect $\mathcal{O}(\epsilon_\mu)$ terms and remain only with $\mathcal{O}(\epsilon_s)$. We also neglect the fluid's shear stresses and assume that there is only a radial distribution of loading pressure. Accordingly, we will use the following approximated form for $\hat{\sigma}_{rr}$ and $\hat{\sigma}_{rr}$:

$$\hat{\sigma}_{rr} \approx -\hat{p}_s - \epsilon_s\hat{p}_d, \quad \text{and} \quad \hat{\sigma}_{r\theta} \approx 0, \quad \text{at} \quad \hat{r} \to \lambda, \tag{45}$$

where $\hat{p}_s(\lambda_0) = \lambda_0^{-2}\mathrm{d}\hat{\psi}/\mathrm{d}\lambda_0$, $\hat{\psi} = \psi/s_1$, and $\epsilon_s\hat{p}_d(\theta;T)$ is the non-uniform perturbation. Ben-Haim et al. (2022) derived the following solution to $\hat{p}_d$

$$\hat{p}_d(\theta;T) = -\frac{\hat{q}\lambda_0}{\epsilon_a^4}\sum_{n=1}^{\infty}\frac{(2n+3)\left((n+1)\tilde{\Lambda}_n^{(in)} + \tilde{\varphi}_{n+1}^{(in)}\right)}{n}\left[\frac{1}{2}\mathbb{P}_n^{(in)} + \mathcal{P}_n(\cos\theta)\right]. \tag{46}$$

Here, $\mathcal{P}_n(\xi)$ is the Legendre function of the first kind of order n, $\{\tilde{\Lambda}_n^{(in)}, \tilde{\varphi}_{n+1}^{(in)}\}$ are the Fourier coefficients given in Appendix D.2, and $\mathbb{P}_n^{(in)}$ is the 0^{th} moment of $\mathcal{P}_n$ about the origin that is defined in Eq. (D.5). Indeed, $\hat{p}_d \sim \mathcal{O}(1)$ close to the shell, as required for our asymptotic analysis.[4]

5.1. Numerical results

We recall that for the intermediate configuration, Eq. (19) provides the relation between $\hat{p}_s$ and λ_0, for any constitutive law of the form (10). Here, by way of example, we present in Fig. 4(a) the pressure–stretch curve of the *Mooney–Rivlin* shell, for the set of parameters that is given in Table 1. This typical curve of the model is a non-monotonic function of the stretch (Beatty, 1987; Ogden, 1972). Here, we focus on the state $\lambda_0 = 1.2$, marked in Fig. 4(a) by the red dot. The corresponding first-order pressure that evolves at the inner surface is presented in Fig. 4(b), as a function of θ. Specifically, the solid black- and dashed red lines present the analytical solution [Eq. (46)] and a finite elements solution using the commercial software COMSOL. In this finite element simulation, the exact equations that describe the fully-coupled problem were solved, using COMSOL's fluid–structure interaction module. In this module, the Navier–Stokes equation governs the flow of entrapped fluid, while the solid was simulated using the solid Mechanics (not the shell or membrane) interface with the Mooney–Rivlin material model. The inlet highlights the variation of $\hat{p}_d$ over $0 < \theta < \theta_f$ (where $\theta_f \approx 2.9$ radians for our set of parameters and $\hat{q} = 0.93$). Note that the slope of this variation becomes very sharp near θ_f, which corresponds to the domain of the inner solution, where the boundary layer emerges.

[3] For details on the derivation of Eq. (40), the reader is referred to the work of Ben-Haim et al. (2022).

[4] For more details on the analytical solution, see Appendix D.4.

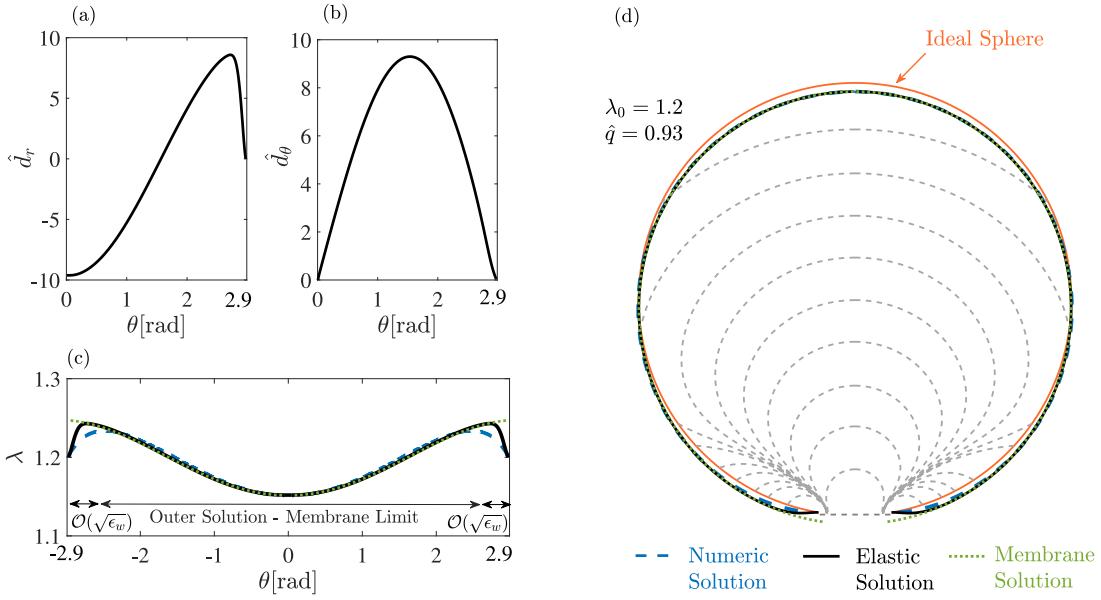

Fig. 5. The relative (a) radial- and (b) tangential displacements, $\hat{d}_r$ and $\hat{d}_\theta$, as functions of θ, obtained by solving Eqs. (26)–(27) with Matlab's numerical integration. (c) The radial stretch of the body. Solid black and dotted green curves denote our Matlab solution and the analytical solution in the membrane limit to the approximation $\lambda(\theta) \sim \lambda_0 + \epsilon_s \hat{d}_r(\theta) + \mathcal{O}(\epsilon_s^2)$. Dashed blue curve denotes the numerical solution obtained via COMSOL. The boundary layer thickness is $\mathcal{O}(\epsilon_w^{1/2})$, in agreement with our analysis. (d) Illustration of the deformation in the Cartesian plane, with the same legend as in panel (c). Contour lines of constant pressure are denoted by dotted gray lines, showing the high-pressure gradient at the entrance.

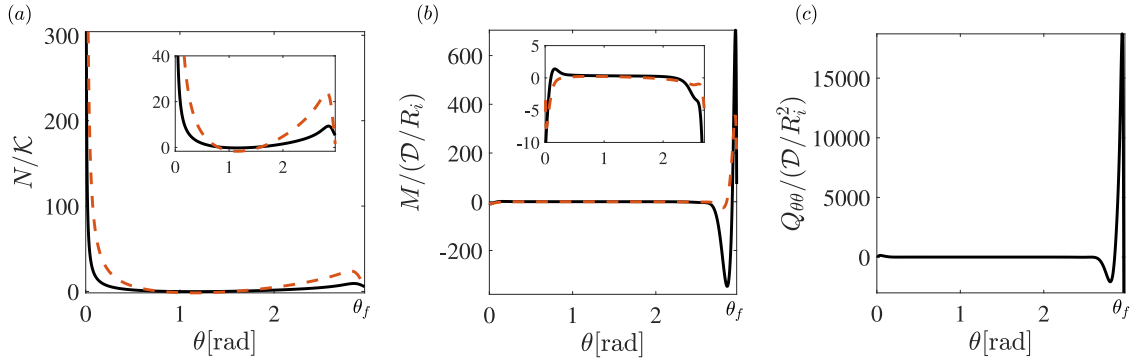

Fig. 6. (a) Tangential force- (solid black $N_{\theta\theta}$ and dashed red $N_{\phi\phi}$); (b) couples- (solid black $M_{\theta\theta}$ and dashed red $M_{\phi\phi}$); and (c) transverse shear resultant $Q_{\theta\theta}$, normalized by the extensional rigidity, bending rigidity over R_i, and bending rigidity over R_i^2, respectively.

Fig. 5 presents the resultant deformations of the shell, owing the non-uniform pressure. Specifically, panels (a) and (b) show the radial- and tangential displacements, $\hat{d}_r$ and $\hat{d}_\theta$, as functions of θ, whose solution was obtained by solving Eqs. (26)–(27) using Matlab's numerical integration.

Panel (c) presents the non-uniform stretch of the body. Here, the solid black- and dotted green curves correspond to our analytical solutions and its membrane limit [Eq. (34)], and the dashed blue curve corresponds to the numerical solution obtained via COMSOL. Note the excellent agreement between the numerical and analytical results, except near the fixed ends of the shell, there we identify the boundary layer by the sharp gradient of the stretch. The boundary layer thickness is $\mathcal{O}(\epsilon_w^{1/2})$, in agreement with our analysis in Section 4.2. The difference between the results is due to the fact that near the tube (*i*) shear stresses are no longer negligible; (*ii*) the drastic stress fluctuations are inconsistent with our regular approximations [Eq. (8)].

Panel (d) presents a better visualization of the resultant shell, by evaluating the deformation in the Cartesian plane [same legend as in panel (c)]. We also present contour lines of constant pressure with dotted gray lines. In the vicinity of the connection with the tube, the contour lines are dense, indicating a high-pressure gradient; these contour lines become more sparse away from the tube, and hence the pressure field decays towards the upper part of the shell.

We proceed to analyze the kinetics of the system, and begin by presenting in Fig. 6 the normalized force resultants [panel (a)], normalized couples [panel (b)], and shear force resultant [panel (c)]. The tangential force resultants are normalized by the extensional rigidity, and the shear force resultants and couples are normalized by the bending rigidity. The solid black line in panels (a) and (b) represent tangential resultant/couples, and the dashed red line represents azimuthal resultant/couples. The results agree with our assumption that the role of the shear force and couples are negligible relative to the tensile force outside the boundary layer.

Finally, we analyze in Fig. 7 the dependency of the flow rate and the finite stretch on the first-order stretch. The former is shown in panel (a), where the solid blue, dashed red, dotted green, and dash-dotted purple curves, correspond to $\hat{q} = 4.66, 2.33, -2.33$ and -4.66, respectively. We observe that the first-order deformation is larger at higher flow rates. Counterintuitively, we further observe that the deflation (inflation) of the shell tends to extend (contract) it in the vertical direction, and contract (extend) it in the horizontal direction.

The dependency of the first-order stretch on λ_0 is shown in panel (b). Specifically, the thick solid orange, dashed azure, dashed–dotted maroon, and thin dotted yellow curves correspond to $\lambda_0 = 1.1, 1.5, 1.7$ and 2, respectively. We observe that at larger finite stretches, the first-order deformations became larger too, a trend that is independent of

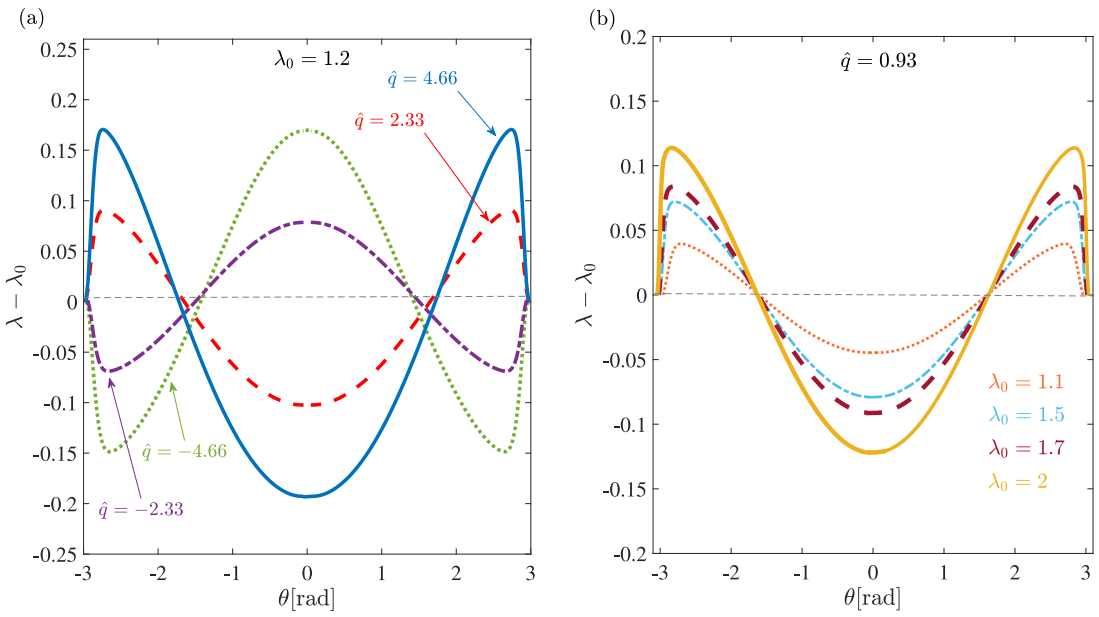

Fig. 7. (a) First order stretch $(\lambda - \lambda_0)$ as a function of θ for $\hat{q} = 4.66, 2.33, -2.33$ and -4.66, denoted by solid blue, dashed red, dotted green, and dash-dotted purple curves, respectively, when $\lambda_0 = 1.2$. (b) First order stretch on as a function of θ for $\lambda_0 = 1.1, 1.5, 1.7$ and 2, denoted by the thickest solid orange, dashed azure, dashed–dotted maroon, and thin dotted yellow curves, respectively, when $\hat{q} = 0.93$.

the flow rate, as we verified using additional calculations (not shown here, for brevity).

6. Summary and concluding remarks

Elastic shells are used in various devices such as pumps, actuators, soft robots, and catheters. Their actuation mechanism is often based on the injection or ejection of fluid to- and from the volume they encapsulate. Such processes lead to non-spherical deformations of the shell, whose modeling is an intricate task, owing to its nonlinear mechanics.

In this work, we developed a framework for modeling these deformations by combining elements from both nonlinear continuum mechanics and structural mechanics. We began by modeling the non-spherical deformation as a superposition of incremental displacements relative to a large spherical deformation. Our motivation for this decomposition stems from the nature of the transient traction that the fluid exerts in the process, namely, that its deviation from spherical uniformity is of order of magnitude smaller than its total magnitude. By doing so, we were able to employ classical nonlinear solutions for the spherical deformation, and utilize the theory of small-on-large, in order to obtain the equations that govern the incremental deformation. This linearization about the finite deformation shows that the structural rigidity of the shell is higher at larger stretch ratios.

In the last stage of our modeling, we developed governing equations in a manner similar to Kirchhoff–Love shell theory. We found that the solution to the resultant balance equations has a boundary layer structure. We identified the leading-order terms of these equations with tensile rigidity and the first-order terms with bending rigidity. We derived an analytical solution to the leading-order part of the equations, which is the dominant part away from the fixed ends of the shell. We determined this characteristic distance from the ends using the method of dominant balance of order of magnitude.

We employed our framework to analyze the non-spherical deformation of the fluid-filled shell that was considered by Ben-Haim et al. (2022). For this parametric example, we derived numerical solutions to our asymptotic equation using Matlab, and carried out fully-coupled finite element simulations using COMSOL Multiphysics. We found that these solutions are in excellent agreement with our analytical solution in the membrane limit, i.e., when the distance from the fixed ends is greater than the characteristic distance that we found. Our numerical study showed that the deviation from the spherical state is larger when the volume of the incoming flow is larger. Our study further showed that the deflation (inflation) of the membrane tends to extend (contract) it in the vertical direction, and contract (extend) it in the horizontal direction, contrary with a naive intuition. Collectively, the framework developed here and the observations that were made based on its numerical application, promote the understanding of the mechanics of such fluid-filled finitely deformed shells and membranes.

Declaration of competing interest

The authors declare that they have no known competing financial interests or personal relationships that could have appeared to influence the work reported in this paper.

Data availability

No data was used for the research described in the article.

Acknowledgments

We thank anonymous reviewers for constructive feedback that helped improve this paper.

Appendix A. The second derivative of the strain energy function and general form of the fourth-order elasticity tensor in terms of the two principal invariants

Owing to relation (10), the first derivative of $\hat{\psi}$ with respect to $\mathbf{C}$ is

$$\frac{\partial \hat{\psi}}{\partial \mathbf{C}} = \frac{\mathrm{d}\hat{\Psi}}{\mathrm{d}I_1}\mathbf{I} + \left(I_1\mathbf{I} - \mathbf{C}\right)\frac{\mathrm{d}\hat{\varphi}}{\mathrm{d}I_2}. \tag{A.1}$$

Moreover, the second derivative, $\partial^2\hat{\psi}/\partial\mathbf{C}^2$, is a fourth-order elasticity tensor. The most general form of the fourth-order elasticity tensor [mentioned in Eq. (9b)] in terms of the two principal invariants is given by Holzapfel (2000)

$$\frac{\partial^2 \hat{\psi}}{\partial \mathbf{C}^2} = \beta_1\mathbf{I}\otimes\mathbf{I} + \beta_2(\mathbf{I}\otimes\mathbf{C} + \mathbf{C}\otimes\mathbf{I}) + \beta_3\mathbf{C}\otimes\mathbf{C} + \beta_4\mathbb{I}, \tag{A.2}$$

where $(\mathbb{I})_{ijk\ell} = \delta_{ik}\delta_{j\ell}$ denotes the fourth-order identity tensor, δ_{ij} is the regular Kronecker delta, and the coefficients $\beta_{1,2,3,4}$ are defined by

$$\beta_1 = \frac{\partial^2\hat{\psi}}{\partial I_1^2} + 2I_1\frac{\partial^2\hat{\psi}}{\partial I_1\partial I_2} + \frac{\partial\hat{\psi}}{\partial I_2} + I_1^2\frac{\partial^2\hat{\psi}}{\partial I_2^2}, \qquad \beta_2 = -\frac{\partial^2\hat{\psi}}{\partial I_1\partial I_2} - I_1\frac{\partial^2\hat{\psi}}{\partial I_2^2},$$
$$\beta_3 = \frac{\partial^2\hat{\psi}}{\partial I_2^2} \quad \text{and} \quad \beta_4 = -\frac{\partial\hat{\psi}}{\partial I_2}. \tag{A.3}$$

Since the deformation gradient is a symmetric tensor in the leading spherical case, $\mathbf{F}_0 = \mathbf{F}_0^T$, it allows us to rewrite the last term of (9b) as follows

$$2\mathbf{F}_0\frac{\partial^2\hat{\psi}}{\partial\mathbf{C}^2}\Big|_{\mathbf{C}_0}\mathbf{C}_1\mathbf{F}_0^T = 4\left(\frac{\mathrm{d}^2\hat{\psi}}{\mathrm{d}I_1^2} + \frac{\mathrm{d}\hat{\varphi}}{\mathrm{d}I_2}\right)\mathrm{tr}\left(\mathbf{F}_0\mathbf{e}\mathbf{F}_0^2\right)\mathbf{F}_0 - 4\frac{\mathrm{d}\hat{\varphi}}{\mathrm{d}I_2}\mathbf{F}_0^2\mathbf{e}\mathbf{F}_0^2, \tag{A.4}$$

where the tracing map is used for obtaining the later relation, as follows

$$(\mathbf{I}\otimes\mathbf{I})\mathbf{A} = (\mathbf{e_i}\otimes\mathbf{e_i}\otimes\mathbf{e_j}\otimes\mathbf{e_j})A_{st}(\mathbf{e_s}\otimes\mathbf{e_t}) = A_{st}\delta_{js}\delta_{jt}(\mathbf{e_i}\otimes\mathbf{e_i})$$
$$= A_{jj}(\mathbf{e_i}\otimes\mathbf{e_i}) = (\mathrm{tr}\mathbf{A})\mathbf{I}, \tag{A.5}$$

for some general second-order tensor $\mathbf{A}$ and right-handed and orthogonal basis $\{\mathbf{e_i}\}$.

Appendix B. Some explicit expressions

The explicit expressions for the effective Young modulus $\tilde{E}(\lambda_0)$, and Poisson ratio $\tilde{\nu}(\lambda_0)$, are

$$\tilde{E}(\lambda_0) = \frac{4\left(\lambda_0^4\hat{\psi}_1 + \hat{\psi}_2\right)\left[2(\lambda_0^3-1)^2(\lambda_0^6+\lambda_0^3+1)\hat{\psi}_{11} + \lambda_0^4(1+\lambda_0^6)\hat{\psi}_1 + \lambda_0^3(2\lambda_0^9 - 2\lambda_0^6 + 5\lambda_0^3 - 2)\hat{\psi}_2\right]}{\lambda_0^2\left[(\lambda_0^3-1)^2(\lambda_0^6+\lambda_0^3+1)\hat{\psi}_{11} + \lambda_0^4(1+\lambda_0^6)\hat{\psi}_1 + \lambda_0^3(\lambda_0^9 - \lambda_0^6 + 3\lambda_0^3 - 1)\Omega_2\right]}, \tag{B.1a}$$

$$\tilde{\nu}(\lambda_0) = \frac{(\lambda_0^3-1)^2(\lambda_0^6+\lambda_0^3+1)\hat{\psi}_{11} + \lambda_0^4\hat{\psi}_1 + \lambda_0^3(\lambda_0^9 - 2\lambda_0^6 + 2\lambda_0^3 - 1)\hat{\psi}_2}{(\lambda_0^3-1)^2(\lambda_0^6+\lambda_0^3+1)\hat{\psi}_{11} + \lambda_0^4(1+\lambda_0^6)\hat{\psi}_1 + \lambda_0^3(\lambda_0^9 - \lambda_0^6 + 3\lambda_0^3 - 1)\hat{\psi}_2}, \tag{B.1b}$$

where

$$\hat{\psi}_{ij} \equiv \frac{\partial^2\hat{\psi}}{\partial I_i\partial I_j}\Big|_{\left(I_1^{(0)},I_2^{(0)}\right)}; \qquad i,j = 1,2, \tag{B.2}$$

and $\hat{\psi}_i$ is defined in (14), (see Fig. 8).

The explicit stress resultants and couples, in terms of the non-spherical displacements, are given by Naghdi and Kalnins (1962)

$$N_{\theta\theta} = \mathcal{K}\left[\frac{1}{\eta_0}\left(d_r + \frac{\mathrm{d}d_\theta}{\mathrm{d}\theta}\right) + \frac{\nu}{\eta_0}\left(d_r + d_\theta\cot\theta\right)\right],$$
$$N_{\phi\phi} = \mathcal{K}\left[\frac{\nu}{\eta_0}\left(d_r + \frac{\mathrm{d}d_\theta}{\mathrm{d}\theta}\right) + \frac{1}{\eta_0}\left(d_r + d_\theta\cot\theta\right)\right],$$
$$M_{\theta\theta} = \mathcal{D}\left[\frac{1}{\eta_0^2}\left(\frac{\mathrm{d}d_\theta}{\mathrm{d}\theta} - \frac{\mathrm{d}^2d_r}{\mathrm{d}\theta^2}\right) + \frac{\nu}{\eta_0^2}\left(d_\theta - \frac{\mathrm{d}d_r}{\mathrm{d}\theta}\right)\cot\theta\right], \tag{B.3}$$
$$M_{\phi\phi} = \mathcal{D}\left[\frac{\nu}{\eta_0^2}\left(\frac{\mathrm{d}d_\theta}{\mathrm{d}\theta} - \frac{\mathrm{d}^2d_r}{\mathrm{d}\theta^2}\right) + \frac{1}{\eta_0^2}\left(d_\theta - \frac{\mathrm{d}d_r}{\mathrm{d}\theta}\right)\cot\theta\right],$$

where $\mathcal{K} = Ew/(1-\nu^2)$ is the extensional rigidity and $\mathcal{D} = Ew^3/12(1-\nu^2)$ is the bending rigidity. The expression of the shear stress resultant $Q_{\theta\theta}$ are (Beuthe, 2008)

$$Q_{\theta\theta} = -\frac{\mathcal{D}}{\eta_0^3}\frac{\mathrm{d}}{\mathrm{d}\theta}\left(\frac{\mathrm{d}^2d_r}{\mathrm{d}\theta^2} + \cot\theta\frac{\mathrm{d}d_r}{\mathrm{d}\theta} + 2d_r\right). \tag{B.4}$$

Note that the expressions shown in relations (B.3) and (B.4) are in their dimensional form.

Appendix C. Technical details for obtaining the equations governing the non-spherical axisemmetric displacements from the balance equation

A compatibility equation can be calculated by eliminating d_θ from the shell strains and replacing the strains with their stress equivalent using the first two equations in (23):

$$\tan\theta\frac{\mathrm{d}}{\mathrm{d}\theta}\left(N_{\phi\phi} - \nu N_{\theta\theta}\right) + \left(\sec^2\theta + \nu\right)N_{\phi\phi} + \left(1 - \nu\sec^2\theta\right)N_{\theta\theta}$$
$$= \frac{Ew}{\eta_0}\left(\frac{\mathrm{d}d_r}{\mathrm{d}\theta} + d_r\tan\theta\right)\tan\theta. \tag{C.1}$$

Following Naghdi and Kalnins (1962) and Sammoura et al. (2014), we define a new stress-function $F(\theta)$, without direct physical interpretation, which serves to define the stress resultants without introducing the tangential displacements. The stress-function satisfies the following relations:

$$N_{\theta\theta} = F + \cot\theta\frac{\mathrm{d}F}{\mathrm{d}\theta} + \frac{1}{\eta_0^3}\mathcal{D}\mathcal{T}_\theta d_r, \quad N_{\phi\phi} = F + \frac{\mathrm{d}^2F}{\mathrm{d}\theta^2} + \frac{1}{\eta_0^3}\mathcal{D}\mathcal{T}_\theta d_r. \tag{C.2}$$

where $\mathcal{D} = Ew^3/12(1-\nu^2)$ is the bending rigidity and $\mathcal{T}_\theta$ is a linear differential operator defined in (28). The tangential displacement d_θ can be related to the radial displacement d_r, by elimination of d_θ from (24b) as

$$d_\theta = \left[\frac{\eta_0}{Ew}\left(N_{\phi\phi} - \nu N_{\theta\theta}\right) - d_r\right]\tan\theta. \tag{C.3}$$

It is possible to obtain the following differential equation by combining the shell strains with (24b), the shear stress resultant (B.4) and the stress function defined in (C.2), to obtain

$$\left[\mathcal{T}_\theta - (1+\nu)\right]F = \frac{Ew}{\eta_0}d_r - (1-\nu)\frac{1}{\eta_0^3}\mathcal{D}\mathcal{T}_\theta d_r. \tag{C.4}$$

This second differential equation can be reached by substituting the resultant of the shear stress (B.4) into the radial momentum Eq. (24a) along with the stress function (C.2),

$$\mathcal{T}_\theta F = \eta_0(p - p_s) - \frac{1}{\eta_0^3}\mathcal{D}\mathcal{T}_\theta^2 d_r. \tag{C.5}$$

Next, we will separate one equation that governs the radial displacement. First, we subtract the Eqs. (C.4) from (C.5) and eliminate the stress function depending only on the radial deformation as

$$(1+\nu)F = \eta_0(p - p_s) - \frac{Ew}{\eta_0}d_r + \frac{1}{\eta_0^3}\mathcal{D}\left[\left((1-\nu) - \mathcal{T}_\theta\right)\mathcal{T}_\theta\right]d_r. \tag{C.6}$$

Now, substitute (C.6) back into the Eq. (C.5) will lead to differential equation that governs the radial deformation, as follow

$$\left[\mathcal{D}\mathcal{T}_\theta^3 - 2\mathcal{D}\mathcal{T}_\theta^2 + \eta_0^2(1-\nu^2)\mathcal{K}\mathcal{T}_\theta\right]d_r = \eta_0^4\left[\mathcal{T}_\theta - (1+\nu)\right](p - p_s), \tag{C.7}$$

where $\mathcal{K} = Ew/(1-\nu^2)$ is the extensional rigidity. In order to eliminate the tangential displacement, d_θ, we start from the substitution of (C.2) in (C.4)–(C.5) to obtain

$$d_\theta = -(1+\nu)\frac{\eta_0}{Ew}\frac{\mathrm{d}F}{\mathrm{d}\theta}. \tag{C.8}$$

Substitute (C.8) back into the relation (C.4), and use some algebraic simplification manipulation will lead to the equation which governs the tangential displacement as follow,

$$\left[\mathcal{T}_\theta - (1+\nu)\right]d_\theta = -(1+\nu)\frac{\mathrm{d}d_r}{\mathrm{d}\theta} + \frac{1}{\eta_0^2}\frac{\mathcal{D}}{\mathcal{K}}\frac{\mathrm{d}}{\mathrm{d}\theta}\mathcal{T}_\theta d_r. \tag{C.9}$$

The equation obtained in (C.9) displays that the tangential displacement depends on the solution of the radial displacement, which must first be determined. Also, the bending can be neglected in the leading order as expected.

We consider examining again the linear relation obtained in Eq. (22) and returning to dimensional variables using the relations (3a)-(3b). From the order of magnitude, the effective Young's modulus must be normalized by $E = \psi^*\tilde{E}(\lambda_0)$ and also $\nu = \tilde{\nu}(\lambda_0)$.

Appendix D. Analytical investigation of the flow-field within an expanding shell

The dynamics problem of a flow within an expanding shell was studied by Ben-Haim et al. (2022). Their results suggest that the pressure distribution can be used as an "external pressure" that causes non-spherical axisymmetric deformations. Here, for completeness, we recall the main results of that work.

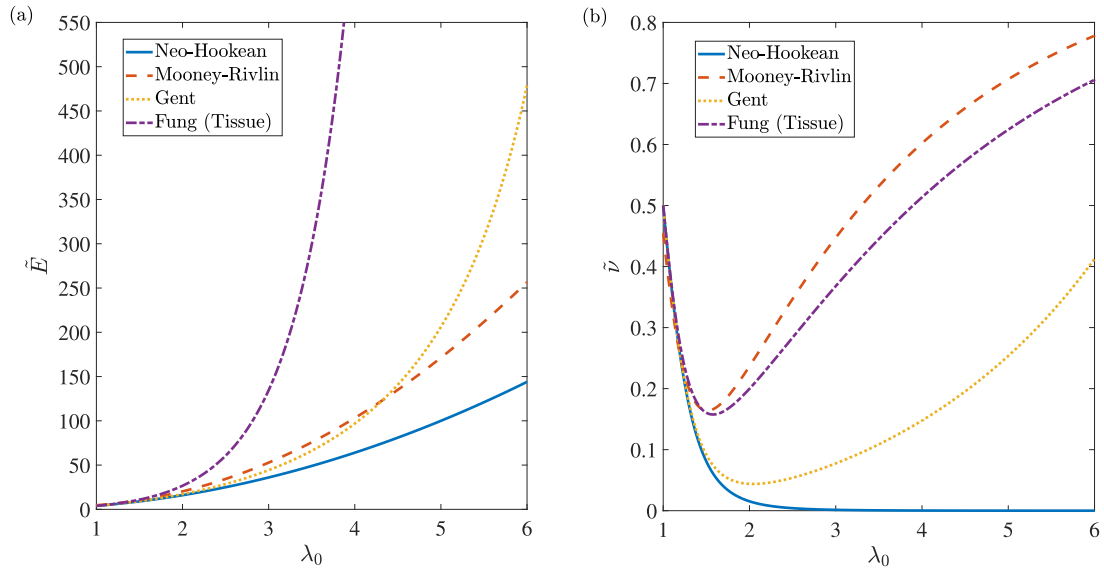

Fig. 8. (a) The effective Young's modulus depends on the stretch of the leading order according to Eq. (B.1a), and (b) the effective Poisson ratio depends on the stretch of the leading order according to Eq. (B.1b). The solid blue, dashed red, dotted yellow, and dashed–dotted purple curves denoted to Treloar (1943), Mooney (1940), Gent (1996), and Fung model for Biological-Tissue (Fung, 1967), respectively.

D.1. Governing equations

In view of tube's slenderness, we assume a constant pressure gradient. We consider negligible gravity, i.e., $\rho g r_0/p^* \ll 1$ (where g is the gravitational acceleration), and assume that the Reynolds number is small. The fluid's motion is governed by Stokes equations for creeping flow with an implicit time variable,

$$\hat{\nabla}\cdot\hat{\boldsymbol{v}}=0,\quad \hat{\nabla}\hat{p}=\epsilon_{\mu}\hat{\nabla}^2\hat{\boldsymbol{v}}. \tag{D.1}$$

D.2. Flow field solution of hyperelastic spherical shell

Based on the assumption of spherical deformation, an analytical series solution is presented, describing the velocity field inside the spherical body, namely,

$$\begin{aligned}\hat{v}_R &= \frac{1}{2}\sum_{n=2}^{\infty}\left[\left((n+2)\chi_0^{-2}-n\right)\Lambda_{n-1}+\left(\chi_0^2-1\right)\varphi_n\right]\chi_0^n\mathcal{P}_{n-1}(\cos\theta),\\ \hat{v}_\theta &= \frac{1}{2}\sum_{n=2}^{\infty}\left[\left(\chi_0^{-2}-1\right)n(n+2)\Lambda_{n-1}+\left(n(1-\chi_0^{-2})+2\right)\varphi_n\right]\chi_0^n\frac{\mathcal{J}_n(\cos\theta)}{\sin\theta},\end{aligned} \tag{D.2}$$

where $\hat{v}_R$ and $\hat{v}_\theta$ are the radial and tangential velocity components, respectively, $\chi_0(\hat{r};T)=\hat{r}/\lambda_0(T)$, and $\mathcal{J}_n(\xi)$ are the *Gegenbauer* functions of the first kind of order n (and degree $-1/2$). The relation with the corresponding Legendre functions of the first kind $\mathcal{P}_n(\xi)$ as,

$$\mathcal{J}_n(\xi)=\frac{\mathcal{P}_{n-2}(\xi)-\mathcal{P}_n(\xi)}{2n-1}=-\frac{1}{(n-1)!}\left(\frac{\mathrm{d}}{\mathrm{d}\xi}\right)^{n-2}\left(\frac{\xi^2-1}{2}\right)^{n-1};\qquad n\geqslant 2. \tag{D.3}$$

In the degenerate cases $n=0,1$ we define $\mathcal{J}_0(\xi)=1$ and $\mathcal{J}_1(\xi)=-\xi$, respectively. In addition, the constants $\Lambda_n(T)$ and $\varphi_n(T)$ represent the general Fourier coefficients of the boundary conditions which defined by Eqs.(4.25)–(4.26) in Ben-Haim et al. (2022).

D.3. Pressure distribution

The pressure distribution of the fluid is,

$$\hat{p}_{(I)}(\hat{r},\theta;T)=\frac{1}{\lambda_0^2}\frac{d\hat{\psi}}{d\lambda_0}-\frac{\epsilon_{\mu}}{\lambda_0}\sum_{n=1}^{\infty}\frac{(2n+3)\big((n+1)\Lambda_n+\varphi_{n+1}\big)}{n}\left[\frac{1}{2}\mathbb{P}_n^{(in)}+\chi_0^n\mathcal{P}_n(\cos\theta)\right], \tag{D.4}$$

where $\mathbb{P}_n^{(\cdot)}$ is the zeroth moment of $\mathcal{P}_n(\xi)$ about an origin, defined as

$$\mathbb{P}_n^{(in)}\equiv\int_{-1}^{-\sqrt{1-\tilde{\epsilon}^2}}\mathcal{P}_n(\xi)\mathrm{d}\xi=\frac{\mathcal{P}_{n+1}\big(-\sqrt{1-\tilde{\epsilon}^2}\big)-\mathcal{P}_{n-1}\big(-\sqrt{1-\tilde{\epsilon}^2}\big)}{2n+1}. \tag{D.5}$$

D.4. Asymptotic justification for using the analytical solution of the pressure distribution obtained in Ben-Haim et al. (2022)

We assume that the pressure distribution inside the body can be described asymptotically as follows:

$$\hat{p}=\hat{p}_s+\epsilon_s\hat{p}_d+\mathcal{O}(\epsilon_s^2)\quad\text{at}\quad\hat{r}\to\lambda, \tag{D.6}$$

where $\hat{p}_s$ is a large uniform part, and $\epsilon_s\hat{p}_d$ is a small order non-uniform perturbation. Therefore, the real shape of the shell consists of an ideal sphere with a small perturbation. According to the numerical results, the perturbation of the shell's stretch is also $\mathcal{O}(\epsilon_s)$, so we assume an asymptotic approximation in the following manner:

$$\lambda(\theta;T)=\lambda_0(T)+\epsilon_s\lambda_1(\theta;T)+\mathcal{O}(\epsilon_s^2). \tag{D.7}$$

We use a regular asymptotic approximation by setting the radial perturbation (D.7) in the general solution of the pressure distribution (D.6), followed by the Taylor expansion, which is approximated as follows:

$$\hat{p}\big(\hat{r}=\lambda(\theta;T)\big)\sim\hat{p}_s\big(\lambda_0(T)\big)+\epsilon_s\hat{p}_d\big(\lambda_0(T),\theta\big)+\mathcal{O}(\epsilon_s^2), \tag{D.8}$$

which has the same loading structure as we assumed in Eq. (4). Moreover, the $\mathcal{O}(\epsilon_s)$ term in the body's shape produces the $\mathcal{O}(\epsilon_s^2)$ pressure correction. In light of these distinctions, we assume a spherical shell and utilize the non-uniform pressure distribution obtained. Then, by the elastic analysis presented in this work, we determine what non-spherical elastic deformations were added to the spherical shape as a result of the small pressures created during the dynamic procedure.

References

Adkins, J.E., Rivlin, R.S., 1952. Large elastic deformations of isotropic materials IX. The deformation of thin shells. Philos. Trans. R. Soc. London Ser. A, Math. Phys. Sci. 244 (888), 505–531.

Akita, D., Saito, Y., Goto, K., Nakashino, K., Matsuo, T., Matsushima, K., Hashimoto, H., Shimadu, S., 2018. Development of a new super-pressure balloon with a net for high-altitude and long-duration flights. Trans. Japan Soc. Aeronaut. Space Sci., Aerosp. Technol. Japan 16 (6), 470–475.

Baek, S., Gleason, R.L., Rajagopal, K., Humphrey, J., 2007. Theory of small on large: potential utility in computations of fluid–solid interactions in arteries. Comput. Methods Appl. Mech. Engrg. 196 (31–32), 3070–3078.

Beatty, M.F., 1987. Topics in finite elasticity: Hyperelasticity of rubber, elastomers, and biological tissues—With examples. Appl. Mech. Rev. 40 (12), 1699.

Ben-Haim, E., Ilssar, D., Or, Y., Gat, A.D., 2022. Viscous flow fields in hyperelastic chambers. J. Fluid Mech. 937.

Ben-Haim, E., Salem, L., Or, Y., Gat, A.D., 2020. Single-input control of multiple fluid-driven elastic actuators via interaction between bistability and viscosity. Soft Robotics 7 (2), 259–265.

Beuthe, M., 2008. Thin elastic shells with variable thickness for lithospheric flexure of one-plate planets. Geophys. J. Int. 172 (2), 817–841.

Bortot, E., Shmuel, G., 2018. Prismatic bifurcations of soft dielectric tubes. Internat. J. Engrg. Sci. 124, 104–114.

Brenner, H., 1964. The Stokes resistance of a slightly deformed sphere. Chem. Eng. Sci. 19 (8), 519–539.

Cassels, J., Hitchin, N., et al., 2001. Nonlinear Elasticity: Theory and Applications. Cambridge University Press.

Corneliussen, A.H., Shield, R., 1961. Finite deformation of elastic membranes with application to the stability of an inflated and extended tube. Arch. Ration. Mech. Anal. 7 (1), 273–304.

Coussios, C.C., Roy, R.A., 2008. Applications of acoustics and cavitation to noninvasive therapy and drug delivery. Annu. Rev. Fluid Mech. 40.

DeBotton, G., Bustamante, R., Dorfmann, A., 2013. Axisymmetric bifurcations of thick spherical shells under inflation and compression. Int. J. Solids Struct. 50 (2), 403–413.

Dorfmann, A., Ogden, R.W., 2010. Nonlinear electroelastostatics: Incremental equations and stability. Internat. J. Engrg. Sci. 48 (1), 1–14.

Firouzi, N., Žur, K.K., 2022. On the generalized nonlinear mechanics of compressible, incompressible, isotropic, and anisotropic hyperelastic membranes. Int. J. Solids Struct. 112088.

Flory, A.L., Brass, D.A., Shull, K.R., 2007. Deformation and adhesive contact of elastomeric membranes. J. Polym. Sci. Part B: Polym. Phys. 45 (24), 3361–3374.

Foster, H., 1967. Very large deformations of axially symmetrical membranes made of neo-hookean materials. Internat. J. Engrg. Sci. 5 (1), 95–117.

Fung, Y., 1967. Elasticity of soft tissues in simple elongation. Am. J. Physiol.-Legacy Content 213 (6), 1532–1544.

Gamus, B., Salem, L., Ben-Haim, E., Gat, A.D., Or, Y., 2017. Interaction between inertia, viscosity, and elasticity in soft robotic actuator with fluidic network. IEEE Trans. Robot. 34 (1), 81–90.

Gao, D.Y., Krysko, V.A., 2006. Introduction to Asymptotic Methods. Chapman and Hall/CRC.

Gaudron, R., Murakami, K., Johnsen, E., 2020. Shape stability of a gas cavity surrounded by linear and nonlinear elastic media. J. Mech. Phys. Solids 143, 104047.

Gent, A.N., 1996. A new constitutive relation for rubber. Rubber Chem. Technol. 69 (1), 59–61.

Green, A., 1954. W. Zerna, Theoretical Elasticity. Clarendon Oxford, UK.

Hart-Smith, L., Crisp, J., 1967. Large elastic deformations of thin rubber membranes. Internat. J. Engrg. Sci. 5 (1), 1–24.

Haughton, D., Ogden, R., 1978. On the incremental equations in non-linear elasticity—II. Bifurcation of pressurized spherical shells. J. Mech. Phys. Solids 26 (2), 111–138.

Hines, L., Petersen, K., Sitti, M., 2017. Asymmetric stable deformations in inflated dielectric elastomer actuators. In: 2017 IEEE International Conference on Robotics and Automation. (ICRA), IEEE, pp. 4326–4331.

Holzapfel, A.G., 2000. Nonlinear Solid Mechanics II. John Wiley & Sons, Inc..

Humphrey, J.D., 2013. Cardiovascular Solid Mechanics: Cells, Tissues, and Organs. Springer Science & Business Media.

Ilssar, D., Gat, A.D., 2020. On the inflation and deflation dynamics of liquid-filled, hyperelastic balloons. J. Fluids Struct. 94, 102936.

Inc., C., 2020. COMSOL. URL http://www.comsol.com/products/multiphysics/.

Ismail, U., Rowe, R.A., Cashin, J., Genin, G.M., Zayed, M.A., 2022. Multimodal thrombectomy device for treatment of acute deep venous thrombosis. Sci. Rep. 12 (1), 5295.

Jenkins, C., 2001. Gossamer spacecraft: Membrane and inflatable structures technology for space applications. AIAA. Inc., Reston, VI.

Klughammer, N., Bischof, J., Schnellbächer, N.D., Callegari, A., Lénárt, P., Schwarz, U.S., 2018. Cytoplasmic flows in starfish oocytes are fully determined by cortical contractions. PLoS Comput. Biol. 14 (11), e1006588.

Kulkarni, Y., 2023. Fluctuations of active membranes with nonlinear curvature elasticity. J. Mech. Phys. Solids 105240.

Li, F.Y., Li, X., Zhang, Q., He, X.T., Sun, J.Y., 2022. A refined closed-form solution for laterally loaded circular membranes in frictionless contact with rigid flat plates: Simultaneous improvement of out-of-plane equilibrium equation and geometric equation. Mathematics 10 (16), 3025.

Liu, M., Wang, C., Li, X., 2018. Rigid-flexible contact analysis of an inflated membrane balloon with various contact conditions. Int. J. Solids Struct. 144, 218–229.

Love, A.E.H., 1888. XVI. The small free vibrations and deformation of a thin elastic shell. Philos. Trans. R. Soc. London(A) (179), 491–546.

Manfredi, L., Capoccia, E., Ciuti, G., Cuschieri, A., 2019. A soft pneumatic inchworm double balloon (SPID) for colonoscopy. Sci. Rep. 9 (1), 1–9.

Melnikov, A., Dorfmann, L., Ogden, R.W., 2020. Bifurcation of finitely deformed thick-walled electroelastic spherical shells subject to a radial electric field. Int. J. Non-Linear Mech. 121, 103429.

Milic-Emili, J., Mead, J., Turner, J., Glauser, E., 1964. Improved technique for estimating pleural pressure from esophageal balloons. J. Appl. Physiol. 19 (2), 207–211.

Mooney, M., 1940. A theory of large elastic deformation. J. Appl. Phys. 11 (9), 582–592.

Multiphysics, C., 1998. Introduction to COMSOL multiphysics®. COMSOL Multiphys., Burlington, MA, Accessed Feb 9, 2018.

Naghdi, P.M., Kalnins, A., 1962. On vibrations of elastic spherical shells.

Needleman, A., 1977. Inflation of spherical rubber balloons. Int. J. Solids Struct. 13 (5), 409–421.

Ogden, R.W., 1972. Large deformation isotropic elasticity–on the correlation of theory and experiment for incompressible rubberlike solids. Proc. R. Soc. Lond. Ser. A Math. Phys. Eng. Sci. 326 (1567), 565–584.

Ogden, R.W., 1997. Non-Linear Elastic Deformations. Courier Corporation.

Poilâne, C., Delobelle, P., Lexcellent, C., Hayashi, S., Tobushi, H., 2000. Analysis of the mechanical behavior of shape memory polymer membranes by nanoindentation, bulging and point membrane deflection tests. Thin Solid Films 379 (1–2), 156–165.

Rivlin, R.S., 1948. Large elastic deformations of isotropic materials IV. Further developments of the general theory. Philos. Trans. R. Soc. London Ser. A, Math. Phys. Sci. 241 (835), 379–397.

Sammoura, F., Akhbari, S., Lin, L., 2014. An analytical solution for curved piezoelectric micromachined ultrasonic transducers with spherically shaped diaphragms. IEEE Trans. Ultrason. Ferroelectr. Freq. Control 61 (9), 1533–1544.

Shmuel, G., 2015. Manipulating torsional motions of soft dielectric tubes. J. Appl. Phys. 117 (17), 174902.

Shmuel, G., DeBotton, G., 2013. Axisymmetric wave propagation in finitely deformed dielectric elastomer tubes. Proc. R. Soc. A: Math., Phys. Eng. Sci. 469 (2155), 20130071.

Siéfert, E., Reyssat, E., Bico, J., Roman, B., 2019. Bio-inspired pneumatic shape-morphing elastomers. Nature Mater. 18 (1), 24–28.

Small, M.K., Nix, W., 1992. Analysis of the accuracy of the bulge test in determining the mechanical properties of thin films. J. Mater. Res. 7 (6), 1553–1563.

Srivastava, A., Hui, C.-Y., 2013. Large deformation contact mechanics of long rectangular membranes. I. Adhesionless contact. Proc. R. Soc. A: Math., Phys. Eng. Sci. 469 (2160), 20130424.

Treloar, L., 1943. The elasticity of a network of long-chain molecules—II. Trans. Faraday Soc. 39, 241–246.

Treloar, L.G., 1975. The Physics of Rubber Elasticity. OUP Oxford.

Vasil'Eva, A.B., Butuzov, V.F., Kalachev, L.V., 1995. The Boundary Function Method for Singular Perturbation Problems. SIAM.

Ventsel, E., Krauthammer, T., Carrera, E., 2002. Thin plates and shells: theory, analysis, and applications. Appl. Mech. Rev. 55 (4), B72–B73.

Verron, E., Khayat, R., Derdouri, A., Peseux, B., 1999. Dynamic inflation of hyperelastic spherical membranes. J. Rheol. 43 (5), 1083–1097.

Xiang, Y., Chen, X., Vlassak, J.J., 2005. Plane-strain bulge test for thin films. J. Mater. Res. 20 (9), 2360–2370.

Yamamoto, H., Sekine, Y., Sato, Y., Higashizawa, T., Miyata, T., Iino, S., Ido, K., Sugano, K., 2001. Total enteroscopy with a nonsurgical steerable double-balloon method. Gastrointest. Endosc. 53 (2), 216–220.

Yang, X., Church, C.C., 2005. A model for the dynamics of gas bubbles in soft tissue. J. Acoust. Soc. Am. 118 (6), 3595–3606.

Yang, W., Feng, W., 1970. On axisymmetrical deformations of nonlinear membranes.

Yang, Y.L., He, X., Sun, X.M., Chen, H., Shi, Z.H., Xu, M., Chen, G.Q., Zhou, J.X., 2017. Optimal esophageal balloon volume for accurate estimation of pleural pressure at end-expiration and end-inspiration: An in vitro bench experiment. Intensive Care Med. Exp. 5, 1–12.

Yeoh, O.H., 1993. Some forms of the strain energy function for rubber. Rubber Chem. Technol. 66 (5), 754–771.